AD-A092 215 STD RESEARCH CORP ARCADIA CALIF F/G 20/3
A COMPUTER STUDY OF HIGH MAGNETIC REYNOLDS NUMBER MHD CHANNEL F--ETC(U)
NOV 80 D A OLIVER, T F SWEAN, C D BANGERTER N00014-77-C-0574
UNCLASSIFIED STDR-80-41 NL

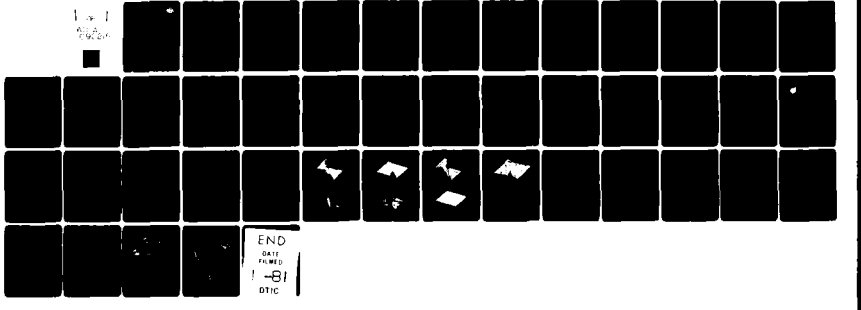

END
DATE FILMED
1-81
DTIC

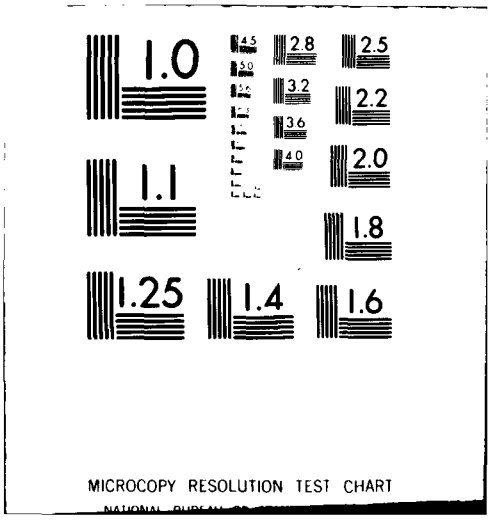
1.0
1.1
1.25
1.4
1.6
1.8
2.0
2.2
2.5
2.8
3.2
3.6
4.0
4.5
5.0
MICROCOPY RESOLUTION TEST CHART

STD RESEARCH CORPORATION

POST OFFICE BOX "C", ARCADIA, CALIFORNIA 91006
TELEPHONE: (213) 357-2311

STDR-80-41

LEVEL II (12)

A COMPUTER STUDY OF HIGH MAGNETIC REYNOLDS NUMBER MHD CHANNEL FLOW

Final Report
Contract No. N00014-77-C-0574

Submitted to

United States Department of the Navy
Office of Naval Research
Arlington, Virginia 22217

October 31, 1980

Approved for Public Release; distribution unlimited

120 West Olive Avenue, Monrovia, California 91016
South California Avenue, Monrovia, California 91016 4724 South 29th Street, Arlington, Virginia 22206

A COMPUTER STUDY OF HIGH MAGNETIC REYNOLDS NUMBER MHD CHANNEL FLOW

by

D. A. Oliver, T. F. Swean, Jr., C. D. Bangerter,
C. D. Maxwell, S. T. Demetriades

Final Report

Contract No. N00014-77-C-0574
Work Unit NR 099-415

Research Sponsored by the
Office of Naval Research

SECURITY CLASSIFICATION OF THIS PAGE (When Data Entered)

14

REPORT DOCUMENTATION PAGE

READ INSTRUCTIONS BEFORE COMPLETING FORM

1. REPORT NUMBER: STDR-80-41	2. GOVT ACCESSION NO.: AD-A092215
	3. RECIPIENT'S CATALOG NUMBER: 9
4. TYPE (and Subtitle): 6 A Computer Study of High Magnetic Reynolds Number MHD Channel Flow.	5. TYPE OF REPORT & PERIOD COVERED: Final rept. 1 Aug 77- 31 Oct 80
	6. PERFORMING ORG. REPORT NUMBER: STDR-80-41
7. AUTHOR(s): 10 D. A. Oliver T. F. Swean, Jr. D. M. Markhasa, C. D. Bangerter and S. T. Demetriades C.D Maxwell	8. CONTRACT OR GRANT NUMBER(s): 15 N00014-77-C-0574
9. PERFORMING ORGANIZATION NAME AND ADDRESS: STD Research Corporation, P. O. Box "C", Arcadia, CA 91006	10. PROGRAM ELEMENT, PROJECT, TASK AREA & WORK UNIT NUMBERS: NR 099-415
11. CONTROLLING OFFICE NAME AND ADDRESS: U. S. Dept. of Navy, Office of Naval Research, Green Street, Pasadena, CA (11)	12. REPORT DATE: 1 Nov 80
	13. NUMBER OF PAGES: 44
14. MONITORING AGENCY NAME & ADDRESS(if different from Controlling Office): (12) 44	15. SECURITY CLASS. (of this report): Unclassified
	15a. DECLASSIFICATION/DOWNGRADING SCHEDULE

16. DISTRIBUTION STATEMENT (of this Report)

Unlimited

17. DISTRIBUTION STATEMENT (of the abstract entered in Block 20, if different from Report)

Unlimited

18. SUPPLEMENTARY NOTES

19. KEY WORDS (Continue on reverse side if necessary and identify by block number)

Magnetohydrodynamic Flow, High Magnetic Reynolds Number Flow, Pulsed MHD Flows.

20. ABSTRACT (Continue on reverse side if necessary and identify by block number)

A summary of progress made in the prediction of magnetogasdynamic phenomena in explosion MHD flows. Theoretical and computational results are presented for quasi-one-dimensional, two-dimensional, quasi-three-dimensional and high Reynolds number flows in both weak and strong MHD interaction.

DD FORM 1 JAN 73 1473 EDITION OF 1 NOV 65 IS OBSOLETE
S/N 0102-LF-014-6601

400046

SECURITY CLASSIFICATION OF THIS PAGE (When Data Entered)

A COMPUTER STUDY OF HIGH MAGNETIC REYNOLDS NUMBER MHD CHANNEL FLOW

1.0 INTRODUCTION

This is a final report describing theoretical and computational studies of the fully coupled motions of a high speed, high temperature plasma flow interacting with an applied magnetid field and an external circuit.

The flows of interest may be created by chemical detonations and the ensuing process may be either inherently unsteady [1] or quasi-steady [2]. In the unsteady process (Fig. 1) the flow consists of a hot plasma ("plasmoid") formed between a driven ionizing shock wave and its following contact surface. The plasmoid is created by a sudden release of energy into a driver section which is in contact with a test gas in which the plasmoid propagates. The conducting plasmoid enters a region in which an externally imposed magnetic field $B^{(0)}$ and electrodes coupled to an external circuit exist (Fig. 1). The plasma conducts current to this external circuit and is subject to Lorentz forces and Joule heating as it propagates through the magnetic field. If the explosion drive is a chemical source, such a plasmoid will be of the order of 5-20 cm in length in traversing a magnetic field region of the order of 100 cm at velocities of the order of 10^4 ms^{-1}. The plasmoid may exist at pressures up to 1 k bar and energies of up to 5 eV.

In a steady flow device, the physical schematic is the same as in Fig. 1 except that a stagnation chamber exists ahead of the MHD channel in which the explosion driven gases are processed. This configuration yields a hypersonic channel flow which is quasi-steady over the flow time scale in the channel.

If $\sigma_0, \rho_0, U_0, B_0$ are the characteristic electrical

conductivity, mass density, velocity, and applied magnetic field, the flow may be specified by an interaction number i and magnetic Reynolds number r_m (in addition to the gasdynamic Mach number):

$$i = \frac{\sigma_0 B_0^2}{\rho_0 U_0} \qquad R_m = \mu_0 \sigma_0 U_0 \tag{1}$$

For an interaction region of length L, the nondimensional numbers are defined as

$$I \equiv \int_0^L i\,dx \qquad R_m \equiv \int_0^L r_m\,dx \tag{2}$$

When $R_m >> 1$, the appropriate measure of the interaction is the parameter S defined as

$$S \equiv (B_0^2/\mu_0)/\langle \rho_0 U_0^2 \rangle \tag{3}$$

where the spatial average $\langle\rangle$ is over the electrically conducting portion of the region L. For a uniform plasmoid of length a, these numbers become $I = \sigma_0 B^2 a/\rho_0 U_0$, $R_m = \sigma_0 \mu_0 U_0 a$, $S = I/R_m$. In the case of a steady flow situation, the characteristic length, a, may be selected as the height of the duct.

It should also be noted that the square of the Alfven Mach number, M_A^2, is equal to the reciprocal of the interaction parameter S (see Appendix A). Thus, electromagnetic effects can nominally propagate upstream ("upstream wakes") for $R_m >> 1$ only for $S \gtrsim 1$ or $M_A \lesssim 1$ (see [3]). By strong interaction we mean flows for which $S \gtrsim 1$ and by high magnetic Reynolds number we mean $R_m \gtrsim 1$.

The primary parameters describing the motion are thus the gasdynamic Mach number M, the interaction parameter S (or I), and the magnetic Reynolds number R_m. In addition, a number of secondary parameters are required to specify the motion.

These include the ratio of electrode length to duct height, and when current flows to the external circuit, the external current parameter $\mathcal{J} \equiv \mu_0 I_c / B_0$ where I_c is the current per unit depth flowing in the external circuit.

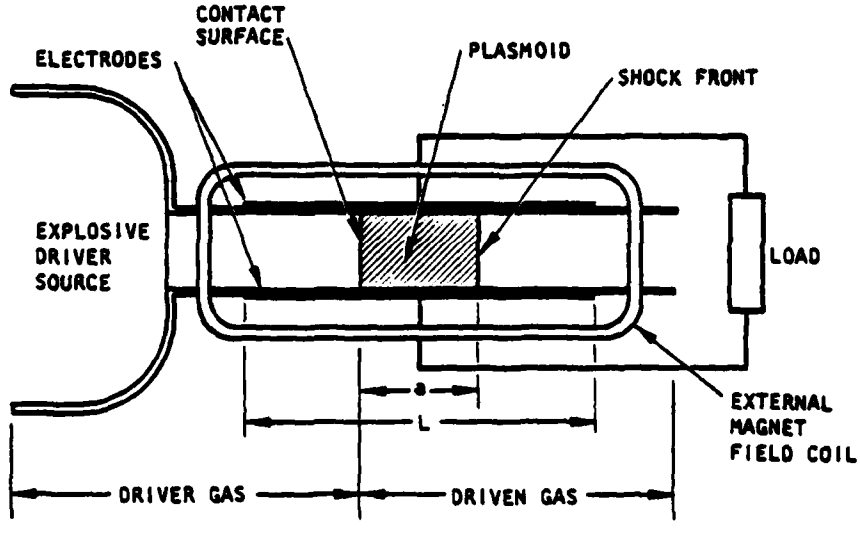

9-2974

Fig. 1. Schematic of explosion-driven plasma flow.

2.0 REVIEW OF PROGRESS

In these studies the authors at STD Research Corporation have presented solutions to a succession of progressively more complex initial value and boundary value problems building up to the strong-interaction, high magnetic Reynolds number motion. Thus in [4], the strong interaction, high magnetic Reynolds number motions were studied in the quasi-one-dimensional approximation. In that work several important phenomena were revealed for the first time. It was shown that under conditions of strong interaction and moderate-to-high magnetic Reynolds numbers the interaction zone progressively decouples from the shock front and evolves into a magneto-hydrodynamic discontinuity (suitably dispersed depending upon the magnetic Reynolds number) which moves at the particle speed of the fluid rather than at the shock front speed. It was further shown in [4] that upstream running shock waves will in general be created in the interaction zone under conditions of large interaction parameters.

In [5] the authors considered the two-dimensional motion under conditions of low to high magnetic Reynolds numbers but under conditions of weak interaction. In this case, the electrical motion is that which results from a two-dimensional, high-speed, turbulent flow proceeding in a constant area duct; since the interaction parameter is vanishingly small the fluid motion is not influenced by the electrical motion. Since there are no geometrical nonuniformities or magnetohydrodynamic forces operating on the fluid, there are no shock wave interactions set up. The principal fluid nonuniformities are the turbulent boundary layers generated on the duct walls. In these studies the detailed eddy-current motions in the non-uniform regions of the applied magnetic field were revealed; but more importantly, the current distribution within the conducting fluid resulting from the electrode system and the external circuit current were also revealed. In particular it

was shown that for magnetic Reynolds numbers in the range $10 < R_m < 20$ the current flowing between the electrodes is convected fully downstream of the electrode gap. As a result, the Lorentz forces which would act on the fluid exist downstream of (and not within) the interelectrode gap. It was further shown that even for electrode systems which are maintained such that the electrode edges do not extend into the fringe field of the applied magnetic field, there is still considerable coupling of the fringe field induced eddy-cells and the electrode system, particularly when the external circuit is open.

In [5] the authors studied a quasi-three-dimensional description of the strong interaction-high magnetic Reynolds number regime. There it was shown that the Lorentz forces concentrated in the magnetic boundary layers under strong interaction conditions would stall these boundary layers and establish a recirculation cell system in the duct with a central jet of plasma which would be relatively free of Lorentz forces. Because of the restrictions of the quasi-three-dimensional model, the reflected-upstream moving shock waves as well as the details of the recirculation cells cannot be described. Only the onset of stall and recirculation can be predicted.

3. RESEARCH PUBLICATIONS

The following publications have originated from the present research:

D. A. Oliver, T. F. Swean, Jr., and D. M. Markham, "Magnetohydrodynamics of Hypervelocity Pulsed Flows" to appear in the AIAA Journal, (1980)

D. A. Oliver, T. F. Swean, Jr., D. M. Markham, C. D. Maxwell, and S. T. Demetriades, "High Magnetic Reynolds Number and Strong Interaction Phenomena in MHD Channel Flows," Proc., 7th Int'l. Conf. on MHD Electrical Power Generation, MIT, Cambridge, MA, June 1980

D. A. Oliver, T. F. Swean, Jr., D. M. Markham and S. T. Demetriades, "Strong Interaction Magnetogasdynamics of Shock-Generated Plasma," AIAA 18th Aerospace Sciences Meeting, Pasadena, CA, Paper No. AIAA-80-0027, January 1980

D. A. Oliver, T. F. Swean, Jr., D. M. Markham, C. D. Bangerter and S. T. Demetriades, "Magnetogasdynamic Phenomena in Pulsed MHD Flows," STD Research Corporation Interim Summary Report No. STDR-79-8 prepared for Office of Naval Research, October 1979

S. T. Demetriades, D. M. Markham, C. D. Maxwell, D. A. Oliver and T. F. Swean, Jr., "Magnetogasdynamic Phenomena in Pulsed MHD Flows," STD Research Corporation Interim Summary Report No. STDR-79-2 prepared for Office of Naval Research, January 1979

S. T. Demetriades, D. M. Markham, C. D. Maxwell, D. A. Oliver and T. F. Swean, Jr., "Magnetogasdynamic Phenomena in Pulsed MHD Flows," Paper presented at ONR Nonideal Plasma Workshop, Pasadena, CA, November 1978

REFERENCES

[1] C. D. Bangerter, B. D. Hopkins and T. R. Brogan, Proc., Sixth Int'l Conf. on Magnetohydrodynamic Electrical Power Generation, Washington, D.C., Vol. IV, p. 155, June 1975

[2] S. P. Gill, D. W. Baum and H. Calvin, "Explosive MHD Research," Artec Assoc. Annual Report No. 119AR to ONR, April 1975 - April 1976

[3] W. R. Sears and E. L. Resler, Jr., "Sub- and Super-Alfvénic Flows Past Bodies," Advances in Aeronautical Science, Vols. 3 and 4, Pergamon Press, London, p. 657, 1962

[4] T. F. Swean, Jr., C. D. Bangerter and D. Markham, "Strong Interaction Magnetogasdynamics of Shock-Generated Plasma," AIAA 18th Aerospace Sciences Meeting, Pasadena, CA, Paper No. AIAA-80-0027, January 1980

[5] D. A. Oliver, T. F. Swean, Jr., D. M. Markham, C. D. Maxwell, and S. T. Demetriades, "High Magnetic Reynolds Number and Strong Interaction Phenomena in MHD Channel Flows," Proc., 7th Int'l. Conf. on MHD Electrical Power Generation, MIT, Cambridge, MA, June 1980

APPENDIX A

THE MATHEMATICAL DESCRIPTION OF MAGNETOGASDYNAMIC FLOWS AT STRONG INTERACTION AND HIGH MAGNETIC REYNOLDS NUMBER

2. THE MATHEMATICAL DESCRIPTION OF MAGNETOGASDYNAMIC FLOWS AT STRONG INTERACTION AND HIGH MAGNETIC REYNOLDS NUMBER

2.1 Fluid Conservation Laws

We may describe the fluid in terms of its mass density, ρ, velocity $\vec{U}$, and internal energy ϵ. We describe the electromagnetic effects in terms of the electric field $\vec{E}$ and magnetic field $\vec{B}$. These variables are considered to be general functions of space $\vec{x}$ and time t. The conservation laws for mass, momentum, and energy are

$$\frac{\partial \rho}{\partial t} + \nabla \cdot (\rho \vec{U}) = 0 \tag{1}$$

$$\frac{\partial}{\partial t}(\rho \vec{U}) + \nabla \cdot (\rho \vec{U}\vec{U}) = \nabla \cdot \vec{\vec{\pi}} + \vec{J} \times \vec{B} \tag{2}$$

$$\frac{\partial}{\partial t}\left[\rho\left(\epsilon + U^2/2\right)\right] + \nabla \cdot \left[\left(\epsilon + U^2/2\right)\rho \vec{U}\right] = \nabla \cdot \left(\vec{\vec{\pi}} \cdot \vec{U}\right) - \nabla \cdot \vec{q} + \vec{J} \cdot \vec{E} \tag{3}$$

In the conservation laws, $\vec{\vec{\pi}}$ is the total pressure tensor and $\vec{q}$ is the heat flux vector. This system of conservation laws is completed in the limit of infinitely fast kinetics by the kinetic and caloric equations of state

$$p = p(\rho, \epsilon) \tag{4}$$

$$\epsilon = \epsilon(p, T) \tag{5}$$

where p is the isotropic part of the stress tensor $\vec{\vec{\pi}}$ and T is the temperature. For a general fluid the state equations, Eqs. (4), (5) cannot be explicitly given but are embedded in the general statistical mechanical description of the equilibrium thermochemistry of the system.

In the case of a perfect gas with particular gas constant R and specific heat ratio γ explicit formulae may be given:

$$p = \rho R T \tag{6}$$

$$\epsilon = (\gamma-1)^{-1} R T \tag{7}$$

$$p = \rho(\gamma-1)\epsilon \tag{8}$$

2.2 The Electromagnetic Contributions

The electrical equations (consisting of the Maxwell equations and the generalized Ohm's law) govern the electric and magnetic fields $\vec{E}, \vec{B}$ and the conduction current density $\vec{J}$. In the hydromagnetic limit these are

$$\nabla \times \vec{E} = - \frac{\partial \vec{B}}{\partial t} \tag{9}$$

$$\nabla \times \vec{B} = \mu_0 \vec{J} \tag{10}$$

$$\nabla \cdot \vec{B} = 0 \tag{11}$$

$$\vec{J} = \sigma \left(\vec{E} + \vec{U} \times \vec{B} \right) + \vec{J}_K \tag{12}$$

where $\vec{J}_K$ is the thermal diffusion flux vector,

$$\vec{J}_K = \sigma \vec{K}$$

and $\vec{K}$ is given by [1]

$$\vec{K} \equiv -\left[\theta^{(1)} \nabla T_e + \theta^{(2)} \nabla T_e \times \vec{B} + \theta^{(3)} (\nabla T_e \times \vec{B}) \times \vec{B} \right.$$

$$\left. - \sum_{\alpha=1}^{N} \left[\beta_\alpha^{(1)} \nabla p_\alpha + \beta_\alpha^{(2)} \nabla p_\alpha \times \vec{B} + \beta_\alpha^{(3)} (\nabla p_\alpha \times \vec{B}) \times \vec{B} \right] \right. \tag{13}$$

The $\theta^{(1)}, \cdots$ and $\beta_\alpha^{(1)} \cdots$ are transport coefficients defined in [1], T_e is the electron temperature and the subscript α denotes a plasma component.

The contributions to the momentum and energy of the system by the electromagnetic field are contained within the Lorentz force, $\vec{J} \times \vec{B}$ and the Lorentz power $\vec{J} \cdot \vec{E}$. The Lorentz force may be represented in terms of the Maxwell stress tensor $\overleftrightarrow{T}$ as

$$\vec{J} \times \vec{B} = \nabla \cdot \overleftrightarrow{T} \tag{14}$$

where the Maxwell stress tensor is defined as

$$\overleftrightarrow{T} = \hat{\mu}_0^{-1} \left(\vec{B}\,\vec{B} - B^2/2\, \overleftrightarrow{I} \right) \tag{15}$$

Correspondingly the Lorentz power may be represented in terms of the Poynting flux $\vec{S}$ and the electromagnetic energy density e_m

$$\vec{J} \cdot \vec{E} = -\nabla \cdot \vec{S} - \frac{\partial e_m}{\partial t} \tag{16}$$

The Poynting flux $\vec{S}$ is defined as

$$\vec{S} = \hat{\mu}_0^{-1}\, \vec{E} \times \vec{B} \tag{17}$$

while the electromagnetic energy density is

$$e_m = \hat{\mu}_0^{-1}\, B^2/2 \tag{18}$$

Let us expand the Poynting flux in terms of $\vec{J}, \vec{B}$ through the use of the Ohm's law

$$\vec{J} = \sigma \left(\vec{E} + \vec{U} \times \vec{B} + \vec{K} \right)$$

We have

$$\vec{S} = \hat{\mu}_0^{-1}\left(\vec{E}\times\vec{B}\right) = \left(\hat{\mu}_0\sigma\right)^{-1}\vec{J}\times\vec{B} - \hat{\mu}_0^{-1}\left(\vec{U}\times\vec{B}\right)\times\vec{B} - \hat{\mu}_0^{-1}\vec{K}\times\vec{B}$$

The term $\vec{J}\times\vec{B}$ is simply $\nabla\cdot\vec{T}$. The term $(\vec{U}\times\vec{B})\times\vec{B}$ is readily shown to be

$$(\vec{U}\times\vec{B})\times\vec{B} = \vec{U}\cdot(\vec{B}\,\vec{B}) - \vec{U}(\vec{B}\cdot\vec{B})$$

which can be rearranged to

$$(\vec{U}\times\vec{B})\times\vec{B} = \vec{U}\cdot(\vec{B}\,\vec{B} - B^2/2\vec{I}) - \vec{U}(B^2/2)$$

The Poynting flux is therefore represented as

$$\vec{S} = e_m\vec{U} - \vec{U}\cdot\vec{T} + \eta\nabla\cdot\vec{T} - \eta\vec{J}_K\times\vec{B} \qquad (19)$$

where $\eta \equiv (\hat{\mu}_0\sigma)^{-1}$ is the magnetic diffusivity. We note that the Poynting flux can be decomposed into four constituent parts: (a) a purely convected flux of electromagnetic energy carried by the motion of the medium ($e_m\vec{U}$); (b) a power flow represented by work done per unit time by the Maxwell stresses acting on the moving medium $-\vec{U}\cdot\vec{T}$; (c) a diffusive flux of electromagnetic energy driven by gradients of the Maxwell stress tensor ($+\eta\nabla\cdot\vec{T}$); and (d) a power flow represented by work done per unit time by the thermal diffusion flux ($-\eta\vec{J}_K\times\vec{B}$).

The electric and magnetic fields and currents may be expressed in terms of vecter potentials $\vec{A}$ and scalar potential Φ as

$$\vec{B} = \nabla\times\vec{A} \qquad (20a)$$

$$\vec{E} = -\nabla\Phi - \frac{\partial\vec{A}}{\partial t} \qquad (20b)$$

2.3 Fluid-Electrical System

The mass, momentum, and energy equations for the general, viscous, hydromagnetic system may now be expressed as

$$\frac{\partial \rho}{\partial t} + \nabla \cdot \vec{M} = 0 \tag{21}$$

$$\frac{\partial \vec{M}}{\partial t} + \nabla \cdot \vec{\Gamma} = \nabla \cdot \vec{\tau} \tag{22}$$

$$\frac{\partial e}{\partial t} + \nabla \cdot \vec{H} = \nabla \cdot (\vec{U} \cdot \vec{\tau}) - \nabla \cdot (\eta \nabla \cdot \vec{T}) - \nabla \cdot \vec{q} + \nabla \cdot (\eta \vec{J}_K \times \vec{B}) \tag{23}$$

In the above $\vec{M} = \rho \vec{U}$ is the momentum density and $\vec{\Gamma}$ is the total fluid and electromagnetic momentum flux

$$\vec{\Gamma} = \rho \vec{U}\vec{U} + p\vec{I} - \vec{T} \tag{24}$$

The total energy density is

$$e = \rho(\epsilon + U^2/2) + e_m \tag{25}$$

and $\vec{H}$ is the total enthalpy flux vector

$$\vec{H} = \left[(e + p)\vec{I} - \vec{T} \right] \cdot \vec{U} \tag{26}$$

The fluid stress tensor $\vec{\pi}$ has been decomposed into a pressure p and viscous stress tensor $\vec{\tau}$ where

$$p = -\frac{1}{3} \text{Trace } (\vec{\pi}) \tag{27}$$

and

$$\vec{\pi} = -p\vec{I} + \vec{\tau} \tag{28}$$

We may define the electromagnetic pressure p_m as the mean normal compressive Maxwell stress:

$$p_m = -\frac{1}{3}\,\mathrm{Trace}(\overleftrightarrow{T}) \tag{29}$$

Expressed in terms of the magnetic field intensity $\vec{B}$, the pressure is

$$p_m = \frac{1}{3}\left(B^2/2\hat{\mu}_0\right) \tag{30}$$

or expressed in terms of the electromagnetic energy density e_m

$$p_m = \frac{1}{3}e_m \tag{31}$$

The Maxwell stress tensor may be decomposed into a magnetic pressure p_m and a Maxwell stress deviator from isotropy $\overleftrightarrow{T}_*$ as

$$\overleftrightarrow{T} = \overleftrightarrow{T}_* - p_m\overleftrightarrow{I} \tag{32}$$

Equation (32) may be thought of as the defining equation for the Maxwell stress deviators $\overleftrightarrow{T}_*$. The *mass*, *momentum*, and energy equations may now be rewritten in alternative form as

$$\frac{\partial\rho}{\partial t} + \nabla\cdot\vec{M} = 0 \tag{33}$$

$$\frac{\partial\vec{M}}{\partial t} + \nabla\cdot\overleftrightarrow{G} = \nabla\cdot\overleftrightarrow{T}_* + \nabla\cdot\overleftrightarrow{\tau} \tag{34}$$

$$\frac{\partial e}{\partial t} + \nabla\cdot\vec{H} = \nabla\cdot(\vec{U}\cdot\overleftrightarrow{T}_*) + \nabla\cdot(\vec{U}\cdot\overleftrightarrow{\tau}) - \nabla\cdot\vec{q} - \nabla\cdot(\eta\nabla\cdot\overleftrightarrow{T}) + \nabla\cdot(\eta\vec{J}_K\times\vec{B}) \tag{35}$$

In the above, $\overleftrightarrow{G}$ is the total momentum flux with only the magnetic pressure included as the magnetic contribution

$$\overleftrightarrow{G} = \rho\vec{U}\vec{U} + (p + p_m)\overleftrightarrow{I} \tag{36}$$

while $\vec{H}$ is the total enthalpy flux consisting of both fluid and electromagnetic pressure and energy contributions.

$$\vec{H} = \left[e + (p + p_m)\right]\vec{U} \tag{37}$$

In terms of the total energy density e, the momentum density $\vec{M}$, and the electromagnetic energy density e_m, the state equations (6) - (8) become

$$p = (\gamma-1)\left[e - e_m - M^2/2\rho\right] \tag{38}$$

$$T = p/\rho R = \frac{(\gamma-1)}{\rho R}\left[e - e_m - M^2/2\rho\right] \tag{39}$$

Let us now consider the transformation of the electrical equations (9)-(12) into more useful forms. Combining Eqs. (9)-(12) we obtain the governing equation for the magnetic induction $\vec{B}$:

$$\frac{\partial \vec{B}}{\partial t} - \nabla \times (\vec{U} \times \vec{B}) = -\nabla \times (\eta \nabla \times \vec{B}) + \nabla \times \vec{K} \tag{40}$$

We note that given the magnetic induction $\vec{B}(\vec{x},t)$ governed by Eq. (40) one immediately has specified the Maxwell stress tensor $\vec{\vec{T}}$ and the electromagnetic energy density e_m. Further, the current density $\vec{J}$ is determined from $\vec{B}$ as

$$\vec{J} = \hat{\mu}_0^{-1} \nabla \times \vec{B}$$

and the electric field $\vec{E}$ as

$$\vec{E} = -\vec{U} \times \vec{B} + \eta \nabla \times \vec{B} - \vec{K}$$

2.4 Viscous and Heat Conduction Effects

Let us now make some observations about the viscous stress tensor $\vec{\vec{\tau}}$ and the heat flux vector $\vec{q}$. The Navier-Stokes moments of the Boltzmann equation yield kinetic theory forms of these quantities:

$$\vec{\vec{\tau}}_L = 2\mu(\vec{\vec{\nabla U}})_0 \tag{41}$$

$$\vec{q}_L = -\lambda \nabla T \tag{42}$$

In the above, μ and λ are the coefficients of viscosity and thermal conductivity and $(\overline{\nabla U})_0$ is the symmetrized, traceless velocity gradient tensor:

$$(\overline{\nabla U})_{0ij} \equiv \frac{1}{2}\left(\frac{\partial U_i}{\partial x_j} + \frac{\partial U_j}{\partial x_i}\right) - \frac{1}{3}\frac{\partial U_k}{\partial x_k}\,\delta_{ij}$$

We denote the stress tensor and heat flux vector with a subscript L to denote that these are laminar quantities. If, on the other hand, we interpret the fluid variables $\rho, \vec{U}, \epsilon, T, \cdots$ as <u>turbulent mean</u> quantities, then $\overline{\overline{\tau}}$ and $\vec{q}$ contain turbulent contributions due to the turbulent velocity and enthalpy correlations. Hence, the complete stress and heat flux fields for a <u>turbulent</u> hydromagnetic medium are

$$\overline{\overline{\tau}} = \langle \rho \vec{U}' \vec{U}' \rangle + \overline{\overline{\tau}}_L$$

$$\vec{q} = \langle \rho \vec{U}' h' \rangle + \vec{q}_R + \vec{q}_L$$

where $\vec{U}', h'$ are the turbulently fluctuating velocity and enthalpy and $\langle\ \rangle$ denotes an ensemble average. A detailed higher order closure theory for the turbulent contributions $\langle \rho \vec{U}' \vec{U}' \rangle$, $\langle \rho \vec{U}' h' \rangle$ is given by Demetriades, Argyropoulos, and Lackner [2]. The radiative heat flux is $\vec{q}_R$. Since the optical depths in dense, explosion generated plasma are so small, the radiative heat flux is only important in layers near the plasma surface of the order of the radiation free path.

2.5 <u>Nondimensional Forms</u>

Let us consider the nondimensionalization of the fluid equations (33) - (35) and the electrical equation (4). For this purpose let us specify characteristic values of the variables as $\rho_0, U_0, \epsilon_0, P_0, T_0, \cdots$ as well as magnetic field B_0. We define a characteristic length L and characteristic time $t_0 = L/U_0$. We indicate nondimensional variables with $\tilde{(\ )}$.

The fluid and electrical conservation laws then become

$$\frac{\partial \tilde{\rho}}{\partial \tilde{t}} + \tilde{\nabla} \cdot \vec{\tilde{M}} = 0 \tag{43}$$

$$\frac{\partial \vec{\tilde{M}}}{\partial \tilde{t}} + \tilde{\nabla} \cdot \vec{\vec{\tilde{\Gamma}}} = R_e^{-1} \tilde{\nabla} \cdot \left[2\tilde{\mu} (\overleftarrow{\tilde{\nabla}} \tilde{U})_0 \right] \tag{44}$$

$$\frac{\partial \tilde{e}}{\partial \tilde{t}} + \nabla \cdot \vec{\tilde{H}} = R_e^{-1} \tilde{\nabla} \cdot \left[2\tilde{\mu} \vec{\tilde{U}} \cdot (\overleftarrow{\tilde{\nabla}} \tilde{U})_0 \right] + \left[(\gamma-1) M^2 R_e P_R \right]^{-1} \tilde{\nabla} \cdot (\tilde{\lambda} \tilde{\nabla} \tilde{T}) -$$

$$- S R_m^{-1} \tilde{\nabla} \cdot (\tilde{\eta} \tilde{\nabla} \cdot \vec{\vec{\tilde{T}}}) - 2S \tilde{\nabla} \cdot (\tilde{\eta} \vec{\tilde{J}}_K \times \vec{\tilde{B}}) \tag{45}$$

$$\frac{\partial \vec{\tilde{B}}}{\partial \tilde{t}} - \tilde{\nabla} \times (\vec{\tilde{U}} \times \vec{\tilde{B}}) = -R_m^{-1} \left\{ \tilde{\nabla} \times (\tilde{\eta} \tilde{\nabla} \times \vec{\tilde{B}}) - \tilde{\nabla} \times (\tilde{\eta} \vec{\tilde{J}}_K) \right\} \tag{46}$$

$$\vec{\tilde{B}} = \tilde{\nabla} \times \vec{\tilde{A}}$$

$$\vec{\tilde{E}} = -\tilde{\nabla} \tilde{\Phi} - \frac{\partial \vec{\tilde{A}}}{\partial \tilde{t}}$$

In the form in which the Maxwell stress tensor is decomposed the left hand sides of the momentum and energy equations take the forms

$$\frac{\partial \vec{\tilde{M}}}{\partial \tilde{t}} + \tilde{\nabla} \cdot \vec{\vec{\tilde{G}}} - S \tilde{\nabla} \cdot \vec{\vec{\tilde{T}}}_* = \frac{\partial \vec{\tilde{M}}}{\partial \tilde{t}} + \tilde{\nabla} \cdot \vec{\vec{\tilde{\Gamma}}}$$

$$\frac{\partial \tilde{e}}{\partial \tilde{t}} + \tilde{\nabla} \cdot \vec{\tilde{H}} - S \tilde{\nabla} \cdot (\vec{\tilde{U}} \cdot \vec{\vec{\tilde{T}}}_*) = \frac{\partial \tilde{e}}{\partial \tilde{t}} + \nabla \cdot \vec{\tilde{H}}$$

The nondimensional variables are defined as

$$\tilde{t} = U_0 t/L \qquad \tilde{\nabla} = L\nabla$$

$$\vec{\tilde{U}} = \vec{U}/U_0$$

$$\tilde{\rho} = \rho/\rho_0$$

$$\vec{\tilde{M}} = \vec{M}/\rho_0 U_0$$

$$\tilde{T} = T/T_0$$

$$\tilde{e} = \tilde{\rho}\left\{\tilde{\epsilon}\left[\gamma\left(\frac{\gamma-1}{2}\right)M^2\right]^{-1} + \tilde{U}^2\right\} + S\,\tilde{e}_m$$

$$\tilde{\epsilon} = \epsilon/[(\gamma-1)^{-1}RT]$$

$$\tilde{e}_m = (B^2/2\hat{\mu}_0)/(B_0^2/2\hat{\mu}_0)$$

$$\vec{\tilde{E}} = \vec{E}/U_0B_0$$

$$\vec{\tilde{B}} = \vec{B}/B_0$$

$$\vec{\tilde{A}} = \vec{A}/(B_0/L)$$

$$\tilde{\Phi} = \Phi/(U_0B_0L)$$

$$\vec{\tilde{J}} = \vec{J}/(\hat{\mu}_0^{-1}B_0/L)$$

$$\vec{\tilde{J}}_K = \vec{J}_K/(\sigma_0U_0B_0)$$

$$\tilde{\tilde{G}} = \tilde{\rho}\vec{\tilde{U}}\vec{\tilde{U}} + \left[(\gamma M^2)^{-1}\tilde{p} + S\tilde{p}_m\right]\tilde{I}$$

$$\tilde{\Gamma} \equiv \tilde{\rho}\vec{\tilde{U}}\vec{\tilde{U}} + (\gamma M^2)^{-1}\tilde{p}\tilde{I} - S\tilde{\tilde{T}}$$

$$\tilde{p}_m = p_m/(B_0^2/2\hat{\mu}_0)$$

$$\vec{\tilde{H}} = \left[\tilde{e} + (\gamma M^2)^{-1}\tilde{p} + S\tilde{p}_m\right]\vec{\tilde{U}}$$

$$\vec{\tilde{H}} \equiv \left[\left(\tilde{e} + (\gamma M^2)^{-1}\tilde{p}\right)\tilde{I} - S\tilde{\tilde{T}}\right]\cdot\vec{\tilde{U}}$$

$$\tilde{\tilde{T}} = \tilde{T}/(B_0^2/2\hat{\mu}_0)$$

$$\tilde{\lambda} = \lambda/\lambda_0 \qquad \tilde{\mu} = \mu/\mu_0 \qquad \tilde{\eta} = \eta/\eta_0$$

where

$$\lambda_0 = \lambda(p_0, T_0), \qquad \mu_0 = \mu(p_0, T_0), \qquad \eta_0 = \eta(p_0, T_0).$$

The state equations (38), (30) in nondimensional form are

$$\tilde{p} = \gamma(\gamma-1)M^2\left[\tilde{e} - S\tilde{e}_m - \tilde{M}^2/\tilde{\rho}\right]$$

$$\tilde{T} = \frac{\tilde{p}}{\tilde{\rho}}$$

It can be seen that the general viscous hydromagnetic equations contain six fundamental nondimensional parameters. These are

M	Mach number	$U_0/(\gamma p_0/\rho_0)^{1/2}$
S	Interaction parameter	$(B_0^2/2\hat{\mu}_0)/(\rho_0 U_0^2)$
R_m	Magnetic Reynolds number	$(U_0 L/\eta_0)$
R_e	Viscous Reynolds number	$\rho_0 U_0 L/\mu_0$
P_R	Viscous Prandtl number	$(C_p \mu_0/\lambda_0)$

We note that the Alfvén speed C_A is defined as

$$C_A = \left(B^2/\hat{\mu}_0\rho\right)^{1/2}$$

and the Alfvén Mach number is $M_A = U/C_A$. Hence the interaction parameter S is also twice the reciprocal of the square of the Alfvén Mach number.

For flows in the absence of viscous and diffusion effects $R_m \to \infty$, $R_e \to \infty$ we obtain the inviscid hydromagnetic equations:

$$\frac{\partial\tilde{\rho}}{\partial\tilde{t}} + \tilde{\nabla}\cdot\vec{\tilde{M}} = 0 \tag{47}$$

$$\frac{\partial\vec{\tilde{M}}}{\partial\tilde{t}} + \nabla\cdot\left[\vec{\tilde{G}} - S\,\vec{\tilde{T}}_*\right] = 0 \tag{48}$$

$$\frac{\partial \tilde{e}}{\partial \tilde{t}} + \nabla \cdot \left[\vec{\tilde{H}} - \vec{\tilde{U}} \cdot \vec{\tilde{T}}_* \right] = 0 \tag{49}$$

$$\frac{\partial \vec{\tilde{B}}}{\partial \tilde{t}} - \tilde{\nabla} \times (\vec{\tilde{U}} \times \vec{\tilde{B}}) = 0 \tag{50}$$

The jump equations across hydromagnetic shocks immediately follow from Eqs. (47)-(50).

$$\left\{ \vec{\tilde{M}} \right\} = 0 \tag{51}$$

$$\left\{ \vec{\tilde{G}} - S \vec{\tilde{T}}_* \right\} = 0 \tag{52}$$

$$\left\{ \vec{\tilde{H}} - \vec{\tilde{U}} \cdot \vec{\tilde{T}}_* \right\} = 0 \tag{53}$$

$$\left\{ \vec{n} \times (\vec{\tilde{U}} \times \vec{\tilde{B}}) \right\} = 0 \tag{54}$$

where $\{\ \}$ denotes the difference in the quantity across the shock surface and $\vec{n}$ is the normal to the shock surface.

Since the electrical conductivity achievable in nonideal plasma is large but finite, the magnetic Reynolds numbers are not infinite but perhaps vary in the range $1 \leq R_m \leq 20$.

In this range, the appropriate system is the inviscid, finite conductivity hydromagnetic system:

$$\frac{\partial \tilde{\rho}}{\partial \tilde{t}} + \tilde{\nabla} \cdot \vec{\tilde{M}} = 0 \tag{55}$$

$$\frac{\partial \vec{\tilde{M}}}{\partial \tilde{t}} + \tilde{\nabla} \cdot \vec{\tilde{\Gamma}} = 0 \tag{56}$$

$$\frac{\partial \tilde{e}}{\partial \tilde{t}} + \tilde{\nabla} \cdot \tilde{\vec{H}} = -SR_m^{-1}\, \tilde{\nabla} \cdot (\tilde{\eta}\, \tilde{\nabla} \cdot \tilde{\tilde{T}}) \tag{57}$$

$$\frac{\partial \tilde{\vec{B}}}{\partial \tilde{t}} - \tilde{\nabla} \times (\tilde{\vec{U}} \times \tilde{\vec{B}}) = -R_m^{-1}\, \tilde{\nabla} \times (\tilde{\eta}\, \tilde{\nabla} \times \tilde{\vec{B}}) \tag{58}$$

or in the alternative form, the momentum and energy equations are

$$\frac{\partial \tilde{\vec{M}}}{\partial \tilde{t}} + \tilde{\nabla} \cdot \tilde{\tilde{G}} = S\, \tilde{\nabla} \cdot \tilde{\tilde{T}}_* \tag{56a}$$

$$\frac{\partial \tilde{e}}{\partial \tilde{t}} + \tilde{\nabla} \cdot \tilde{\vec{H}} = S\, \tilde{\nabla} \cdot (\tilde{\vec{U}} \cdot \tilde{\tilde{T}}_*) - SR_m^{-1} \tilde{\nabla} \cdot (\tilde{\eta}\, \tilde{\nabla} \cdot \tilde{\tilde{T}}) \tag{56b}$$

2.6 Applied and Induced Fields

Let us separate the magnetic field $\vec{B}$ into an applied portion $\vec{B}^{(0)}$ sustained by currents external to the plasma and plasma induced portion $\vec{B}^{(i)}$ which results from currents flowing within the plasma:

$$\vec{B} = \vec{B}^{(0)} + \vec{B}^{(i)} \tag{57}$$

The induction equation, Eq. (58), then becomes

$$\frac{\partial \tilde{\vec{B}}^{(i)}}{\partial \tilde{t}} - \tilde{\nabla} \times (\tilde{\vec{U}} \times \tilde{\vec{B}}^{(i)}) = -R_m^{-1} \left\{ \tilde{\nabla} \times (\tilde{\eta}\, \tilde{\nabla} \times \tilde{\vec{B}}^{(i)}) - \tilde{\nabla} \times (\tilde{\eta}\, \tilde{\vec{J}}_K) \right\}$$
$$-R_m^{-1} \tilde{\nabla} \times (\tilde{\eta}\, \nabla \times \tilde{\vec{B}}^{(0)}) - \tilde{\vec{B}}^{(0)} \tag{58}$$

where $\frac{\partial \tilde{\vec{B}}^{(0)}}{\partial \tilde{t}}$ is denoted $\dot{\tilde{\vec{B}}}^{(0)}$

APPENDIX B

AIAA PAPER AIAA-80-0027

STRONG INTERACTION MAGNETOGASDYNAMICS OF SHOCK-GENERATED PLASMA

D. A. Oliver, T. F. Swean, Jr., D. M. Markham
and S. T. Demetriades

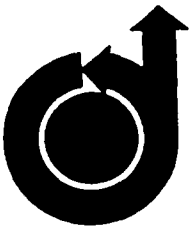

AIAA-80-0027

Strong Interaction Magnetogasdynamics of Shock-Generated Plasma

D. A. Oliver, T. F. Swean, Jr.,
D. M. Markham and S. T. Demetriades,
STD Research Corp., Arcadia, Ca.

AIAA 18th
AEROSPACE SCIENCES MEETING
January 14-16, 1980/Pasadena, California

STRONG INTERACTION MAGNETOGASDYNAMICS OF SHOCK-GENERATED PLASMA

D. A. Oliver, T. F. Swean, D. M. Markham, and S. T. Demetriades
STD Research Corporation
Arcadia, California

Abstract

The magnetohydrodynamic behavior of shock-generated pulses of plasma ("plasmoids") in encounter with an applied magnetic field is studied. Reflection and transmission of the plasmoid shock front is revealed as well as the existence of Joule heated zones which are convectively unstable. It is shown that strong interaction plasmoids are not delimited by shock front and following contact surface; rather, they develop their own internal, evolving structure under the mutual influence of self Joule heating, and induced magnetic field. As a result, the interaction zone behind an ionizing shock wave will progressively decouple from the shock front and follow a trajectory given by the particle motion of the gas rather than the wave motion of the shock front.

I. Introduction

In the present work we study the behavior of shock-generated magnetohydrodynamic flow over the range of weak and strong magnetohydrodynamic interaction and low to high magnetic Reynolds numbers. Such a flow consists of a hot plasma "plasmoid" formed between a driven ionizing shock wave and its following contact surface. The plasmoid is created by a sudden release of energy in a driver section which is in contact with a test gas in which the plasmoid propagates. Such a flow may be driven, for example, by the use of focused chemical explosives[1,2].

The conducting plasmoid enters a region in which an externally imposed magnetic field $\bar{B}_0$ and electrodes coupled to an external circuit exist (Fig. 1). The plasma conducts current to this external circuit and is subject to Lorentz forces and Joule heating as it propagates through the magnetic field. If the explosion drive is a chemical source, such a plasmoid will be of the order of 5-20 cm in length in traversing a magnetic field region of the order of 100 cm at velocities of the order of 10^5 ms^{-1}. The plasmoid may exist at pressures up to 1 k bar and energies of 5 eV.

If σ_0, ρ_0, U_0 are the characteristic electrical conductivity, mass density and velocity within the plasmoid, the flow may be specified by an interaction number per unit length i and magnetic Reynolds number per unit length r_m (in addition to the gasdynamic Mach number).

$$i = \frac{\sigma_0 B_0^2}{\rho_0 U_0} \qquad r_m = \mu_0 \sigma_0 U_0 \tag{1}$$

For an interaction region of length L, the non-dimensional numbers are defined as

$$I = \int_0^L i\,dx \qquad R_m = \int_0^L r_m\,dx \tag{2}$$

When $R_m >> 1$, the appropriate measure of the interaction is the parameter S defined as

$$S \equiv \left(B_0^2/\mu_0\right) / \langle \rho U^2 \rangle \tag{3}$$

where the spatial average $\langle\ \rangle$ is over the electrically conducting portion of the region L. For a uniform plasmoid of length a, these numbers become

$$I = \sigma_0 B_0^2 a/\rho_0 U_0, \quad R_m = \sigma_0 \mu_0 U_0 a, \quad S = I/R_m.$$

Pulsed magnetohydrodynamic flows have been examined in the case of low magnetic Reynolds number ($R_m << 1$) and weak interaction ($I \lesssim 1$)[3,4]. Because of the low interaction, these studies revealed simple current flow through the plasmoid and weak magnetohydrodynamic deceleration.

The transverse ionizing shock wave which forms the front of the plasmoid has been extensively studied in the limit of infinitely large magnetic Reynolds number[5,6,7,8]. In addition to the exposition of the general Rankine-Hugoniot conditions for these shocks[5] it has also been demonstrated tha such shock waves can be reflected as well as transmitted upon encounter with an externally imposed magnetic field. These studies also showed that the electric field in front of the shock must be self-consistently determined with the dynamical state behind the shock and the electrical boundary conditions imposed upon the gas[6].

In the present study, we examine the magnetohydrodynamics of the whole plasmoid in its encounter with, and transit through an externally imposed magnetic field. We show that under conditions of strong interaction, hypervelocity plasmoids can possess a rich variety of magnetohydrodynamic phenomena including magnetically reflected shock waves, embedded MHD discontinuities, and significant periods of transonic flow within the plasmoid. In particular, we reveal the dynamics of reflected and transmitted waves through the plasmoid in both the low and high magnetic Reynolds number regime. We reveal the behavior of electrothermally unstable plasmoids. We show that, in general, the plasmoid is not delimited by the region between the shock front and contact surface. Instead, the plasmoid develops its own internal, evolving structure governed by the mutual interaction of self-heating and induced self-fields.

Shock-generated hypervelocity flows of this kind are subject to a variety of nonideal phenomena. These include wall interaction effects (viscous losses, gas leakage, and ohmic voltage drops in boundary layers), thermal radiation losses, and kinetic/ionization relaxation effects behind shock waves. In the present study we ignore these effects and examine those phenomena which arise specifically from the magnetohydrodynamic

interaction.

In Part II of what follows we present a mathematical description of the flow of quasi-one-dimensional plasmoids. In Part III we examine the dynamics of strong interaction plasmoids with an applied magnetic field but at low magnetic Reynolds number. In Part IV we similarly consider strong interaction plasmoids but at large magnetic Reynolds number. In Part V we illustrate the behavior of "transitional" plasmoids. These are flows in which the plasmoid enters the magnetic field at relatively low values of interaction parameter and magnetic Reynolds number. As a result of self-Joule heating, however, the plasmoid conductance is elevated as it progresses through the field carrying it into the strong interaction, high magnetic Reynolds number regime.

II. Mathematical Description

A. Conservation Laws for Fluid and Electricity

We consider a quasi-one-dimensional description of the gas moving over the spatial coordinate x in time t. Average properties (over the cross-section) of the duct describing the flow are its density ρ, internal energy ε, velocity U, and pressure p. The magnetic field $\vec{B}$ we separate into an applied field $\vec{B}_0$ and a field $\vec{B}_i$ induced by the plasma currents. From these we select the total mass, momentum, and energy densities

$$\left[\rho, m = \rho U,\ e = \rho(\varepsilon + U^2/2) + B_i^2/2\mu_0\right]$$

as the state $\underline{W}(x,t)$ specifying the flow at any point in space and time:

$$\underline{W}(x,t) = \begin{bmatrix} \rho \\ m \\ e \end{bmatrix} \tag{4}$$

The fluid conservation laws are

$$\frac{\partial \underline{W}}{\partial t} = -\frac{\partial \underline{F}}{\partial x} + \underline{\Xi} \tag{5}$$

In the above, $\underline{F}$ represents the convected fluxes of mass, momentum, and energy while $\underline{\Xi}$ contains the Lorentz force and power associated with the applied magnetic field and the Joule dissipation. These are expressed in terms of current density $\vec{J}$ and magnetic field $\vec{B}_0$:

$$\underline{F} = \begin{bmatrix} m \\ m^2/\rho + p + B_i^2/2\mu_0 \\ m/\rho(e + p + B_i^2/2\mu_0) \end{bmatrix} \quad \underline{\Xi} = \begin{bmatrix} 0 \\ (\vec{J}\times\vec{B}_0)_x \\ J^2/\sigma - \vec{J}\cdot(\vec{U}\times\vec{B}_0) \end{bmatrix} \tag{6}$$

In this illustration study we assume that the kinetic effects are confined to the relaxation layer at the shock, and further, that the relaxation layer is thin compared to the overall thickness of the plasmoid.

For the simple geometry (x,y,z) of Fig. 1, the magnetic field $\vec{B}$ is given by $\vec{B}(0,0,B)$, the electric field by $\vec{E} = \vec{E}(0,E,0)$, and the current by $\vec{J} = \vec{J}(0,J,0)$. The description for the near fields J, B_i of the plasmoid is then given by Ohm's law and the Maxwell equation in the MHD approximation:

$$J = \sigma\left(E - UB_i - UB_0\right) \tag{7}$$

$$\frac{\partial B_i}{\partial x} = -\eta\left(E - UB_i - UB_0\right) \tag{8}$$

where $\eta \equiv (\mu_0\sigma)^{-1}$ is the magnetic diffusivity.

External interaction conditions with an external circuit including inductive coupling with the applied magnetic field coil are required to complete the description of actual flow situations. Rather than include such circuit detail in these illustrations we assume that the external circuit is configured so that an electric field $\vec{E} = \vec{E}(0,E,0)$ is maintained within the interelectrode region whose magnitude is uniform in space and given by

$$E = \kappa\langle UB\rangle \tag{9}$$

where κ is a "load" parameter ($0 \le \kappa \le 1$). For a passive external circuit, the value $\kappa = 0$ corresponds to a shorted external circuit; for $\kappa = 1$ the external circuit is open circuited.

The fluid variables ρ, p, T, σ, U are nondimensionalized by the values $\rho_0, p_0, T_0, \sigma_0, U_0$ characterizing the interior of the initial plasmoid before encounter with the magnetic field. Nondimensional space and time $\bar{x}, \bar{t}$ are defined in terms of x, nondimensionalized by the plasmoid length a, and t by a/U_0. The nondimensional parameters governing the interaction are the Mach number M, the gas heat ratio Y, either of the interaction parameters I or S, and the magnetic Reynolds number R_m.

B. Boundary and Initial Conditions

In the limit of $R_m \to \infty$, the system consisting of Eqs. (4) and (7) is fully hyperbolic. For finite R_m, the system is mixed hyperbolic/parabolic with embedded regions where resistive effects occur. The boundary and initial conditions which specify the interaction problem for an explosion generated plasmoid encounter with a magnetic field are as follows. As an initial condition we take an idealized explosion driven flow in which the plasmoid of given breadth a occupies the hot zone between contact surface and shock front[3] (Fig. 3). At time t = 0 the shock front is located at the edge of the magnetic field. Over the time scale for the dynamics of interest the shock front of the plasmoid will run continuously into the quiescent driver gas while the backward running rarefaction continuously runs into the explosive source. Hence the boundary conditions for the fluid equations are those of specified explosion and quiescent states at the boundaries $x = +L_1$, $x = -L_2$ respectively.

The boundary condition for the induced magnetic field B_i from Eq. (8) is that of symmetry across the overall plasmoid so that at $x = L_1$, $x = -L_2$ which lie outside the region of any current flow

$$B_i(-L_2,t) = -B_i(L_1,t)$$

The applied magnetic field B_0 is uniform in both space and time.

C. Numerical Procedures

The solutions to the initial-value problems formulated above and to be discussed in Parts III, IV, and V are computationally generated with second order accurate explicit finite difference operators. The hyperbolic system is treated with the MacCormack version of the Lax-Wendroff-Richtmyer operator[18]. For the space-time grid utilized, comparisons were made with the analytically available solutions for the zero and infinite R_m, zero interaction limits. At the extreme pressure ratios of 10^5 between driver and driven gas for these explosion generated plasmoids, the maximum variations between the computationally generated and analytical solutions within the plasmoid (expressed as a fraction of the analytical solution) are 0.025 in velocity, 0.04 in pressure, and 0.08 in temperature.

III. Interaction at Low Magnetic Reynolds Number

We now proceed to the first of several illustrations of the foregoing description. We consider first the strong interaction of a plasmoid with the magnetic field but at low magnetic Reynolds number. In Fig. 2 the kinematics of this situation are shown. When the incident plasmoid encounters the magnetic field, the leading shock front may be both transmitted and reflected. In the case of reflected fronts, the rear (contact surface) of the plasmoid subsequently interacts with the reflected shock front. This colliding disturbance then radiates a fast and slow reflected shock (denoted shock II) back through the plasmoid (which consists of subsonic flow behind the reflected shock front) where it then collides with the now strongly decelerated shock front.

For the illustration shown here, we select a plasmoid with Mach number M = 1.64, interaction parameters I = 20, S = 200, and Reynolds number R_m = 0.1, just before encountering the magnetic field. The full conditions for the flow are given in Table I. We impose the condition that the electrical conductivity is spatially uniform within the high temperature plasmoid (we consider electrical conductivity functions which are consistently coupled to the gas thermodynamic state in Part V). This uniform conductivity distribution is achieved in the computations with the model conductivity function

$$\sigma = \begin{cases} 0 & T/T_0 < 1/3 \\ \sigma_0 & T/T_0 \geq 1/3 \end{cases}$$

which effectively switches on a constant conductivity σ_0 within the plasmoid and switches the conductivity off outside the zone in which the plasmoid exists. The dynamics of the interaction are exhibited in Figs. 4, 5, and 6. When the plasmoid shock front encounters the magnetic field, it is both reflected and transmitted. The reflected shock I collides with the contact surface and initiates a fast reflected shock II and a slow reflected shock. The fast reflected shock II reestablishes high velocity flow through the plasmoid and reencounters the transmitted shock front which has been decelerated. During this period of strong wave dynamics the current distribution within the plasmoid is strongly affected (Fig. 5). The current is diminished to very small values during the period of plasmoid deceleration behind the reflected shock I, and then returns back to enhanced levels after passage of the fast reflected shock II. The low magnetic Reynolds number of the plasmoid allows the current to diffuse nearly uniformly throughout its breadth.

IV. Interaction at High Magnetic Reynolds Number

We next consider the behavior of a uniform conductivity plasmoid in the high magnetic Reynolds number regime. For this case the incident plasmoid has an interaction parameter I = 20 as in the previous illustration but a magnetic Reynolds number R_m = 5. Correspondingly, the interaction number S has the reduced value S = 4. The full conditions for this flow are given in Table II. The encounter of this plasmoid with the magnetic field is similar to that of Part III. The features peculiar to the higher Reynolds number are best perceived in the current distribution of Fig. 7 which is more nonuniform compared to that of Fig. 8. When the current levels rise behind the reflected shock II, they do so by directly following the shock until it merges with the transmitted front. The current maximum then remains at the shock front of the plasmoid. As a result of decelerating Lorentz forces concentrated immediately behind the shock front, the shock front is slowed and the overall breadth of the plasmoid is decreased as it progresses through the magnetic field. This is in contrast to the plasmoid dynamics of Parts III and V.

V. Transitional Plasmoids

We now turn to consideration of plasmoid behavior with a coupled electrical conductivity model. In contrast to the previous illustrations in which the conductivity is spatially uniform within the high temperature plasmoid and vanishes outside, we consider a conductivity which is appropriately coupled to the thermodynamic state of the gas. As a result, local regions within the plasmoid can be rendered more conductive by the self-Joule heating of the plasmoid. With the electrical conductivity strongly coupled to the Joule dissipation, a plasmoid in the low I, low R_m range can evolve into the large I, large R_m range as it progresses through the magnetic field and experiences further Joule heating. We term such flows "transitional" plasmoids.

We consider a conductivity function of the form

$$\sigma^{-1} = \sigma_{en}^{-1} + \sigma_{ei}^{-1} \tag{10}$$

In the above σ_{en} is an electrical conductivity of a neutral species background and σ_{ei} is the Coulomb conductivity. We use as a summary representation of these two contributions the forms

$$\sigma_{en} = \sigma_0 \left(\frac{T}{T_0}\right)^n \tag{11}$$

$$\sigma_{ei} = 152\, \bar{Z}_{eff}^{-2}\, T^{3/2}/\ell n\Lambda \qquad (12)$$

where $\bar{Z}_{eff}$ is the average effective ionic charge and σ_0, T_0, $\ell n\Lambda$, $n > 0$ are parameters for a given gas.

The conductivity function Eqs. (10)-(12) is dominated by the partially ionized conductivity σ_{en} at low temperature and goes over to the Coulomb (fully-ionized) conductivity at high temperature. This conductivity function has the property $\partial\sigma/\partial T \geq 0$ over the entire range of temperature. Since there are no thermal energy loss mechanisms (which would be principally radiative) included in the model, the plasmoid is unconditionally electrothermally unstable[11,12]. This convective instability is simply a growth of temperature nonuniformities within the plasmoid due to intensifying Joule heating resulting from growing electrical conductivity.

The interaction of a representative transitional plasmoid is shown in Figs. 8-10. This plasmoid has interaction parameters $I = 1$, $S = 1$ and magnetic Reynolds number $R_m = 1$ just before it enters the magnetic field. The complete conditions for this flow are given in Table III. It should be noted that the interaction at entry into the magnetic field is considerably smaller than the interaction described in Parts III and IV. The plasmoid progresses into the field where it begins to self-heat and decelerate. The modest interaction at plasmoid entry to the magnetic field does not create distinct reflected waves, but rather a strong and continuous deceleration. Magnetic Reynolds number and interaction parameter grow significantly has the plasma is heated. At time $\bar{t} = 2.6$, the magnetic Reynolds number is in excess of 10 and the current has progressively become sheet-like. It should be noted that the current maxima no longer follow immediately behind the transmitted shock front. Rather, the current concentrates in the electrothermally heated zone which is then convected at the local fluid speed rather than radiated at the shock front speed. This decelerating electrothermal instability is then swept up by collision with the waves initiated by the arrival of the contact surface at the magnetic field inlet. A feature of note is the development of reversed current flow in the upstream portion of the current sheet due to the sharply diminished magnetic field behind the current sheet at large R_m.

VI. Summary Remarks

In this study we have illustrated significant purely magnetogasdynamic phenomena which occur when a hypervelocity pulse of plasma ("plasmoid") encounters an applied magnetic field under strong interaction conditions. With uniform electrical conductivity within the plasmoid (and vanishing electrical conductivity outside), reflection and transmission of the plasmoid shock front are possible coupled with strongly nonuniform current evolution in time. Such plasmoids with large magnetic Reynolds numbers have current distributions (and decelersting Lorentz forces) concentrated immediately behind the shock front. As a result of shock front deceleration, these plasmoids diminish in breadth as they proceed through the magnetic field. With electrical conductivity within the plasmoid coupled to its thermodynamic state, the plasmoid is electrothermally unstable and creates its own, evolving region of enhanced electrical conductance which carries most of the current and is convected at the fluid speed within the plasmoid. The shock front becomes increasingly free of current and runs progressively farther ahead of the unstable current structure embedded in the plasmoid interior.

Nonideal phenomena such as viscous wall layers, kinetic-relaxation effects behind the shock front, and thermal radiation losses can play important roles in these strong interaction flows. The basic structure of the magnetohydrodynamic interaction itself, however, is a prerequisite to the description and understanding of these additional modifying effects.

VII. Acknowledgements

This work was sponsored by the U.S. Office of Naval Research, Contract No. N00014-77-C-0574.

References

1. M. Jones, "Explosion Driven Linear MHD Generators," Proc. Conf. on Megagauss Magnetic Field Generation by Explosives, Frescati, Italy, Sept. 1965

2. I. I. Glass, S. K. Chan, and H.L. Brode, "Strong Planar Shock Waves Generated by Explosively-Driven Spherical Implosions," AIAA J., Vol. 12, No. 3, March 1974, p. 367

3. J. Rosciezewski and W. Gallaher, "Shock Tube Flow Interaction with an Electromagnetic Field," Proc. Seventh Int'l. Shock Tube Symp. ed. I. I. Glass, Univ. of Toronto, p. 475-489 (1970)

4. J. J. Rosceszewski and T. T. Yeh, "Shock Tube Flow Passing Through a Section of a Linear MHD Generator," AIAA J., Vol. 11, No. 12, p. 1756 (1973)

5. C. K. Chu and Robert A. Gross, "Shock Waves in Plasma Physics," Adv. Pl. Phys. ed. A. Simon and W.B. Thompson, Vol.2,p.139,(1969)

6. C. K. Chu, "Dynamics of Ionizing Shock Waves: Shocks in Transverse Magnetic Fields," Phys. Fluids, Vol. 7, No. 8, p. 1349, August 1964

7. Dmitri A. Bout and Robert A. Gross, Interaction of an Ionizing Shock Wave with a Transverse Magnetic Field," Phys. Fluids, Vol. 13, No. 6, p. 1473, June 1970

8. Dmitri A. Bout, Richard S. Post, and Herman Presby, "Ionizing Shocks Incident Upon a Transverse Magnetic Field," Phys. Fluids, Vol. 13, No. 5, p. 1399, May 1970

9. Ya. B. Zel'dovich and Yu. P. Raizer, Physics of Shock Waves and High Temperature Hydrodynamic Phenomena, Vol. 1, Academic Press, NY, 1966, p. 234-238

10. R. F. Warming, et al., "Second- and Third-Order Noncentered Difference Schemes for Nonlinear Hyperbolic Equations," AIAA J., Vol. 11, No. 2, February 1973

11. D. A. Oliver, "A Constricted Discharge in Magnetohydrodynamic Plasma," Proc. 15th Symposium on Engineering Aspects of Magnetohydrodynamics, Univ. Pennsylvania, Philadelphia, p. IX.4, May 1976

12. S. T. Demetriades, C. D. Maxwell, G. S. Argyropoulos, and G. Fonda-Bonardi, "Influence of Controlled Turbulence on Gaseous Discharges," Proc. 11th Symposium on Engineering Aspects of Magnetohydrodynamics, Caltech, Pasadena, CA, p. 64, March 1970

TABLE I

Conditions for Interaction at Low Magnetic Reynolds Number

T_∞ Quiescent driven gas temperature

P_∞ Quiescent driven gas pressure

$M = 1.64$ $\quad \gamma = 1.5$

$P_0/P_\infty = 232$

$T_0/T_\infty = 45$ $\quad \kappa = 0.5$

TABLE II

Conditions for Interaction at High Magnetic Reynolds Number

$M = 1.64$ $\quad \gamma = 1.5$

$P_0/P_\infty = 232$

$T_0/T_\infty = 45$ $\quad \kappa = 0.5$

TABLE III

Conditions for Transitional Plasmoid

$M = 1.64$ $\quad \theta = 1080$

$P_0/P_\infty = 232$ $\quad n = 3.11$

$T_0/T_\infty = 45$ $\quad Z_{eff}^{-2}/\ell n\Lambda = 0.16$

$\gamma = 1.5$ $\quad \kappa = 0.5$

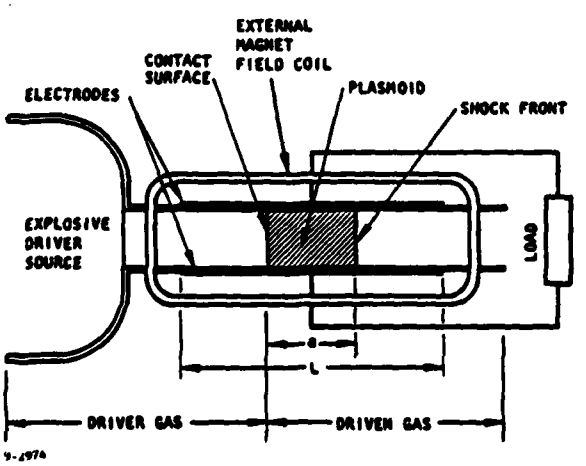

Fig. 1. Schematic of explosion-driven plasmoid flow

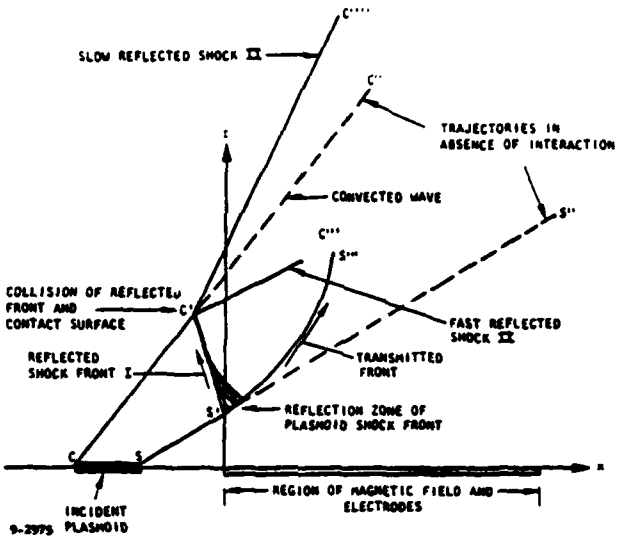

Fig. 2. Space-time diagram of strong interaction hypervelocity plasmoids. Plasmoid trajectory in the limit of vanishing interaction is delimited by the shock front trajectory SS'S'' and contact surface trajectory CC'C''. Plasmoid shock front reflection S'C' and transmission S'S'' are initiated at encounter with magnetic field. Contact surface encounters reflected front at C' which generates fast reflected shock II (C'C'''), slow reflected shock II (C'C''''), and convected wave (C'C'').

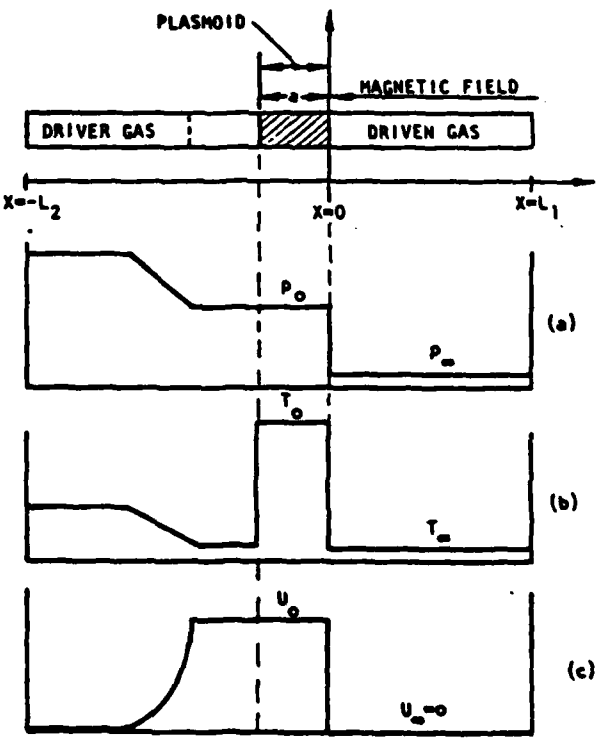

Fig. 3. Initial condition for plasmoid interaction for the pressure (a), temperature (b), and velocity (c). Shock front of plasmoid of given breadth a located at magnetic field edge at time t = 0.

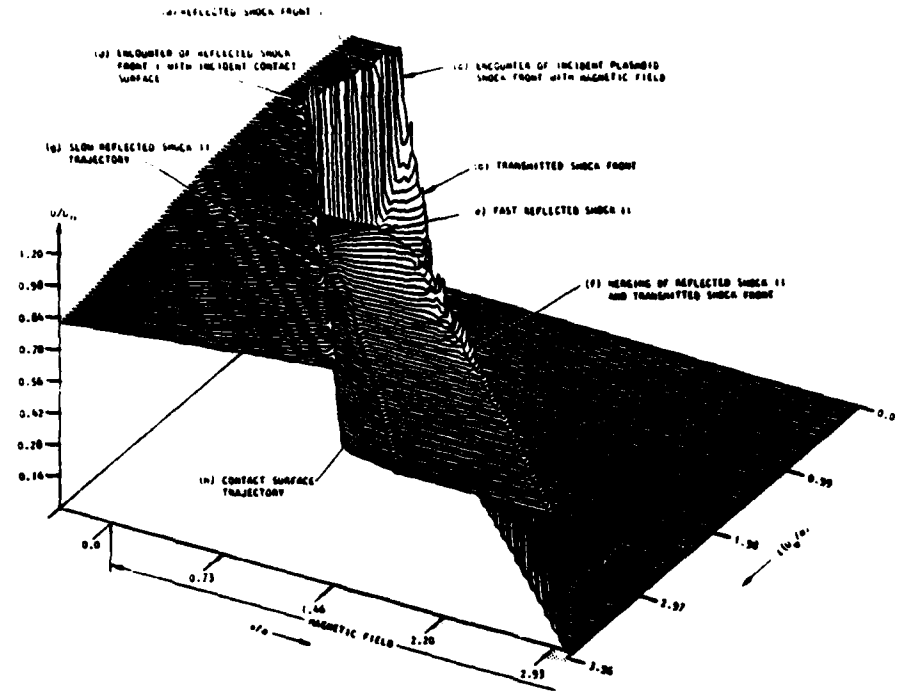

Fig. 4. Velocity field of plasmoid in transit through an applied magnetic field under strong interaction (I = 20), low magnetic Reynolds number (R_m = 0.1) conditions. Shock front of plasmoid is both reflected from magnetic field (a) and transmitted into magnetic field (b). Reflected wave I (a) collides with contact surface (d) and initiates a fast reflected shock II (e) and slow reflected shock (g). Reflected wave II (e) merges with transmitted shock front (f). Contact surface (h) separates conducting from nonconducting gas behind. Note transitory region of sharply diminished velocities within the plasmoid during the period of reflection and rereflection of the shock front.

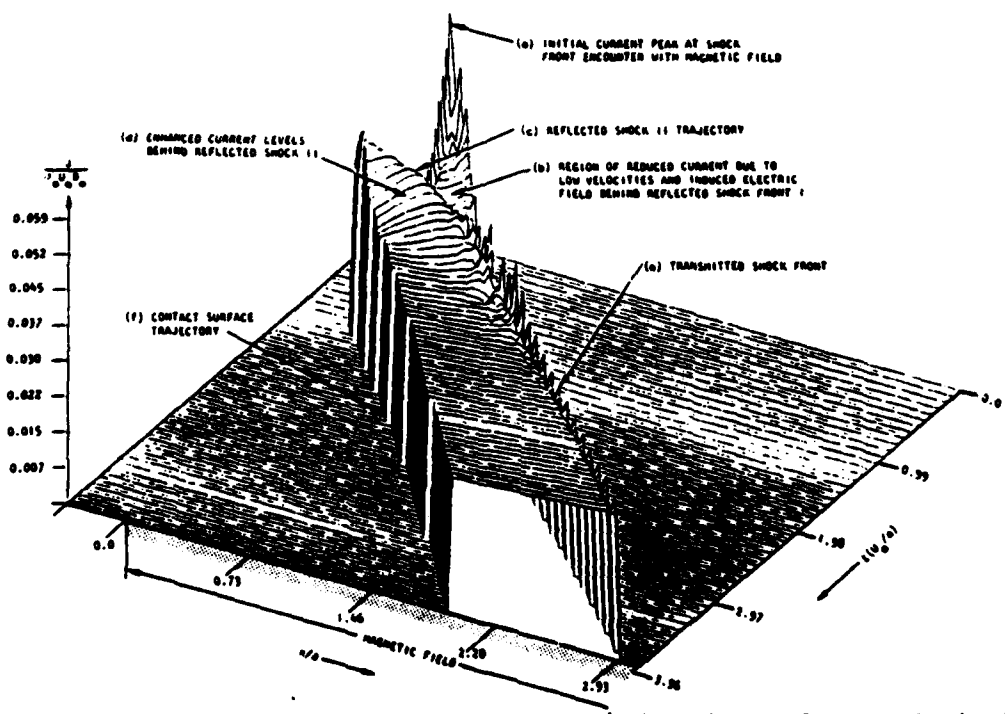

Fig. 5. Current density distribution for conditions of Fig. 4. Initial peak of current density (a) diminishes sharply as plasmoid velocities diminish behind reflected shock front I (b). After passage of reflected shock II (c) current levels rise (d) and remain uniform through plasmoid. With uniform conductivity model, conductivity is uniform between shock front (e) and contact surface (f). At low magnetic Reynolds number (R_m = 0.1), current is diffused nearly uniformly over plasmoid.

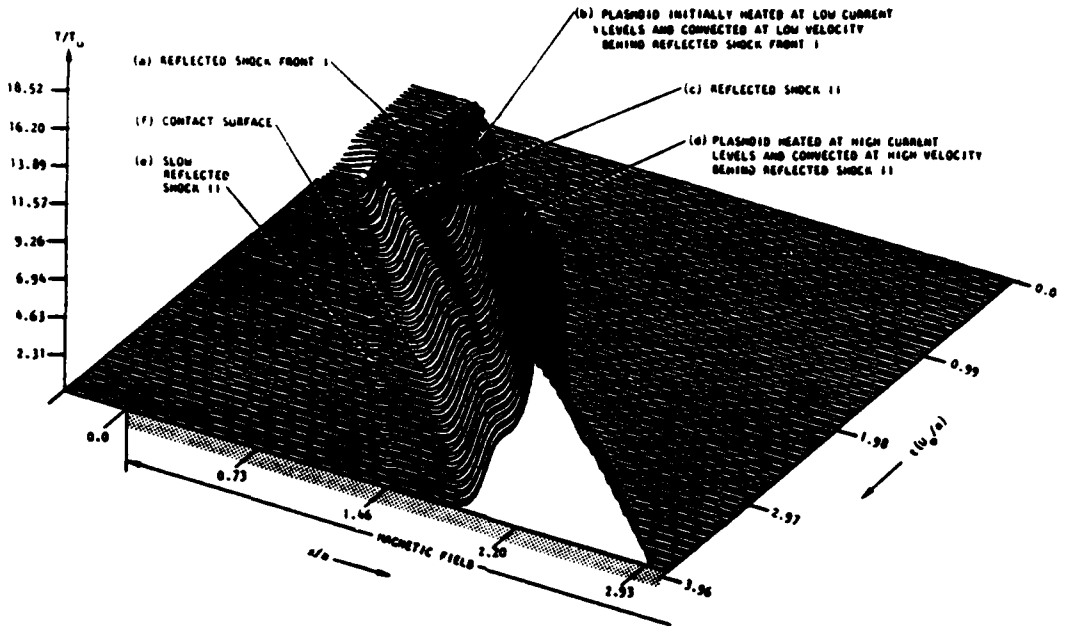

Fig. 6. Temperature distribution for conditions of Fig. 4. Otherwise uniform temperature of plasmoid is affected by wave dynamics, and most significantly, by Joule heating. Weak initial current levels due to reflected shock front I (a) as shown in Fig. 4 lead to weak elevations in temperature due to Joule heating (b). Note that heated region within plasmoid at that time is convected at low velocity. Transmitted shock front is sharply decelerated. Contact surface is much less decelerated during this period. After passage of reflected shock II (c), Joule heating increases significantly thereby elevating plasmoid interior temperature (b). Following passage of reflected shock II, plasmoid interior is convected at velocities ranging between that of front and that of contact surface. Trace (e) is due to the slow reflected shock wave II.

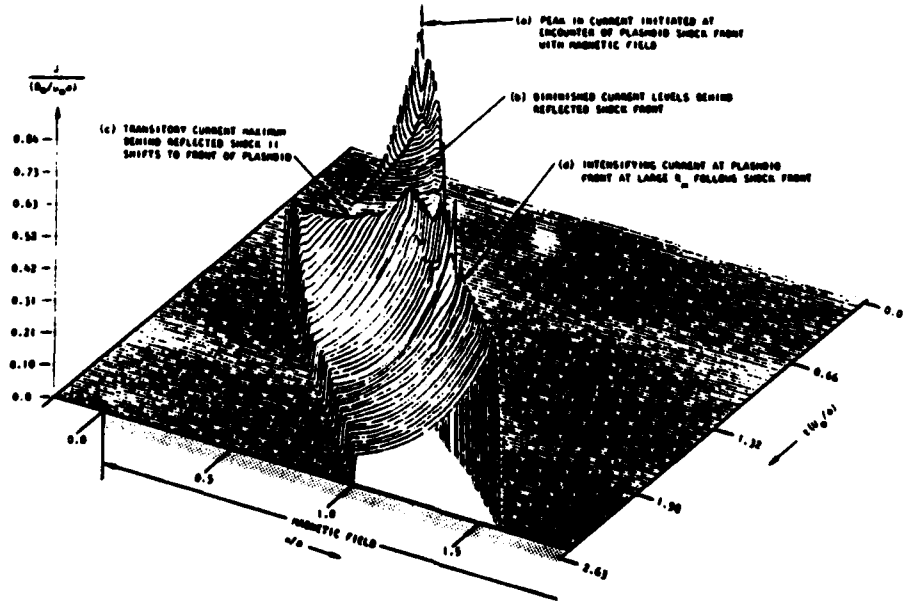

Fig. 7. Current distribution for a strong interaction plasmoid at $R_m = 5$. Dynamics are similar to those exhibited in Figs. 4-6, however the larger Reynolds number permits more nonuniform current (and induced magnetic field) distributions. Current pulse initiated by encounter of plasmoid shock front (a) gives way to diminished current levels in low velocity region behind reflected shock front I (b). Current levels rise and shift to front of plasmoid (c),(d) after passage of reflected shock front II. Note that current concentrates immediately behind shock front in contrast to that of Fig. 5 (where current is nearly uniform) and that of Fig. 10 (where current is nearly absent) behind shock front.

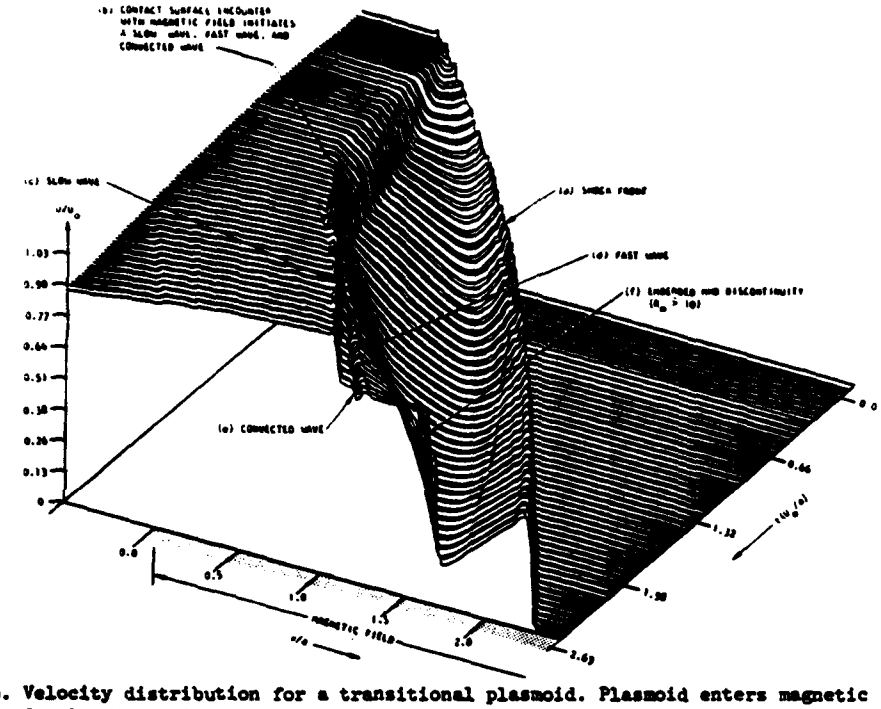

STD 9-2980

Fig. 8. Velocity distribution for a transitional plasmoid. Plasmoid enters magnetic field with I = 1, R_m = 1, S = 1. Modest interaction at entry to magnetic field does not generate distinct reflected waves, but rather strong and continuous deceleration. Magnetic Reynolds number and interaction parameters grow during the course of transit. Shock front proceeds through magnetic field with continuous deceleration (a). Once the Reynolds number reaches values $R_m \geq 10$, the current has become sheet-like with a deflagration-like, intensifying discontinuity within a large subsonic zone of the plasmoid. Contact surface encounter with magnetic field (b) initiates downstream running waves (c), (d), (e).

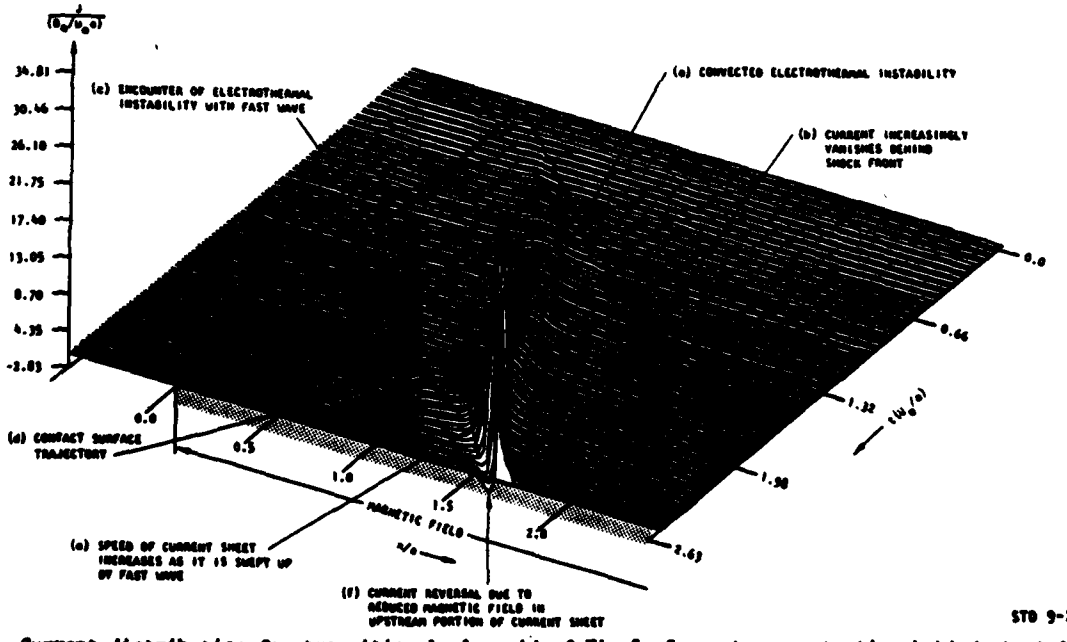

STD 9-2981

Fig. 9. Current distribution for transitional plasmoid of Fig.8. Current concentration behind shock front at entry to magnetic field grows (a) with corresponding heating and conductivity enhancement (reflected in temperature field of Fig.10). Shock front propagates ahead (b), but becomes increasingly free of current. Electrothermally heated zone becomes the most highly conducting region of the plasmoid. This heated zone is convected with the gas and strongly decelerated. Sharp rise in temperature and current occurs when unstably evolving current pulse (which is convected) collides with radiated wave (c). Current pulse is then swept up by contact surface and reaccelerated (e). Note current reversal due to sharply reduced magnetic field in upstream portion of current sheet (f).

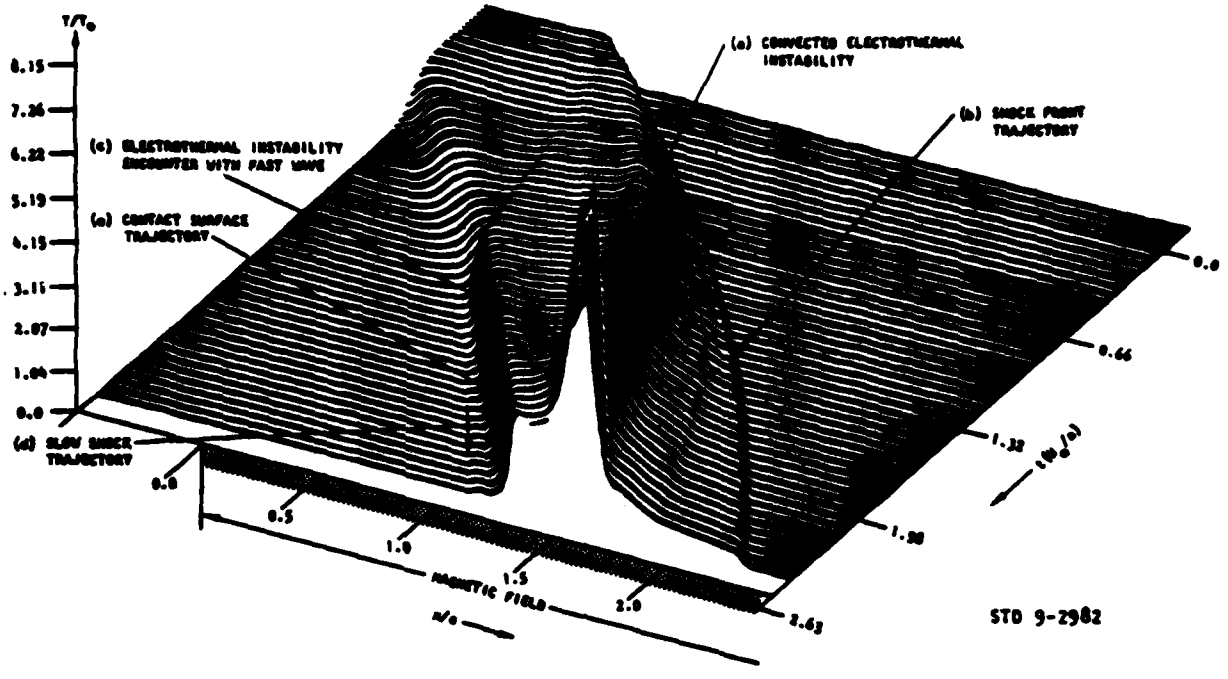

Fig. 10. Temperature field corresponding to Figs. 8,9 showing developing electrothermal instability.

APPENDIX C

HIGH MAGNETIC REYNOLDS NUMBER EFFECTS AND STRONG INTERACTIVE PHENOMENA IN MHD CHANNEL FLOWS

D. A. Oliver, T. F. Swean, Jr., D. M. Markham, C. D. Maxwell
and S. T. Demetriades

HIGH MAGNETIC REYNOLDS NUMBER AND STRONG INTERACTION PHENOMENA IN MHD CHANNEL FLOWS

D. A. Oliver, T. F. Swean, Jr., D. M. Markham, C. D. Maxwell and S. T. Demetriades
STD Research Corporation
Arcadia, California 91006

I. INTRODUCTION

In this paper we examine some phenomena of interest in magnetohydrodynamic (MHD) channel flow at high magnetic Reynolds number. Such flows may be created by chemical explosions and the ensuing MHD process may be either inherently unsteady[1] or quasi-steady.[2]

In the unsteady process (Fig. 1) the flow consists of a hot plasma ("plasmoid") formed between a driven ionizing shock wave and its following contact surface. The plasmoid is created by a sudden release of energy into a driver section which is in contact with a test gas in which the plasmoid propagates. The conducting plasmoid enters a region in which an externally imposed magnetic field $B^{(0)}$ and electrodes coupled to an external circuit exist (Fig. 1). The plasma conducts current to this external circuit and is subject to Lorentz forces and Joule heating as it propagates through the magnetic field. If the explosion drive is a chemical source, such a plasmoid will be of the order of 5-20 cm in length in traversing a magnetic field region of the order of 100 cm at velocities of the order of 10^4 ms^{-1}. The plasmoid may exist at pressures up to 1 k bar and energies of up to 5 eV.

In a steady flow device, the physical schematic is the same as in Fig. 1 except that a stagnation chamber exists ahead of the MHD channel in which the explosion driven gases are processed. This configuration yields a hypersonic channel flow which is quasi-steady over the flow time scale in the channel.

If σ_0, ρ_0, U_0 are the characteristic electrical conductivity, mass density and velocity, the flow may be specified by an interaction number i and magnetic Reynolds number r_m (in addition to the gasdynamic Mach number):

$$i = \frac{\sigma_0 B_0^2}{\rho_0 U_0} \qquad r_m = \mu_0 \sigma_0 U_0 \tag{1}$$

For an interaction region of length L, the nondimensional numbers are defined as

$$I = \int_0^L i\,dx \qquad R_m = \int_0^L r_m dx \tag{2}$$

When $R_m \gg 1$, the appropriate measure of the interaction is the parameter S defined as

$$S = (B_0^2/\mu_0) / \langle \rho U^2 \rangle \tag{3}$$

where the spatial average $\langle\ \rangle$ is over the electrically conducting portion of the region L. For a uniform plasmoid of length a, these numbers become $I = \sigma_0 B^2 a/\rho_0 U_0$, $R_m = \sigma_0 \mu_0 U_0 a$, $S = I/R_m$.

In Part II of what follows we consider two-dimensional electrical conduction under conditions of high R_m for the unsteady flow of a plasmoid and its encounter with the applied magnetic field and the electrode system. In Part III we consider the two-dimensional steady, hypersonic flow of plasma at high magnetic Reynolds number through a constant area rectangular duct. We describe the current distribution in the plasma of Parts II and III under the conditions of high R_m but for vanishing interaction I.

In Part IV we consider the three-dimensional strong interaction dynamics of a steady hydromagnetic channel flow at high magnetic Reynolds numbers. The quasi-one-dimensional, strong-interaction, high R_m unsteady problem is treated in Ref. 3.

II. Unsteady High Magnetic Reynolds Number Electrical Conduction

A. Governing Electrical Equation

Let us now consider the form of the electrical equations. The Maxwell equations and Ohm's law govern the electric field $\vec{E}$, magnetic field $\vec{B}$, and current density $\vec{J}$. Let z be the axis aligned with an applied magnetic field $\vec{B}^{(0)}$ and let x,y be the coordinates defining the plane of conduction. The current vector then becomes $\vec{J} = \vec{J}(\tilde{J}_x, \tilde{J}_y, 0)$, the magnetic vector becomes $\vec{B} = \vec{B}(0,0,\tilde{B})$, and the velocity $\vec{U} = \vec{U}(\tilde{U}_x, \tilde{U}_y, 0)$ where $\vec{J}$ is the current vector nondimensionalized on $B_m^{(0)}/\mu_0 a$. $B_m^{(0)}$ is the maximum value of the applied magnetic field. $\vec{U}$ is the velocity nondimensionalized on the duct inlet velocity U_0. $\vec{B}$ is the magnetic field nondimensionalized on the maximum applied magnetic field $B_m^{(0)}$. We divide the magnetic field into the applied portion $\vec{B}^{(0)}$ and a portion $\vec{B}^{(i)}$ which is induced by the currents flowing in the plasma. The Maxwell equations and Ohm's law then may be combined in the induction equation form as

$$\frac{\partial \tilde{B}^{(i)}}{\partial \tilde{t}} + \frac{\partial}{\partial \tilde{x}}(\tilde{U}_x \tilde{B}^{(i)}) + \frac{\partial}{\partial \tilde{y}}(\tilde{U}_y \tilde{B}^{(i)}) = R_m^{-1}\left[\tilde{\eta}\left(\frac{\partial^2 \tilde{B}^{(i)}}{\partial \tilde{x}^2} + \frac{\partial^2 \tilde{B}^{(i)}}{\partial \tilde{y}^2}\right) + \right. \tag{4}$$

$$\left. + \frac{\partial \tilde{\eta}}{\partial \tilde{x}}\frac{\partial \tilde{B}^{(i)}}{\partial \tilde{x}} + \frac{\partial \tilde{\eta}}{\partial \tilde{y}}\frac{\partial \tilde{B}^{(i)}}{\partial \tilde{y}}\right] - \frac{\partial}{\partial \tilde{x}}(\tilde{U}_x \tilde{B}^{(0)}) - \frac{\partial}{\partial \tilde{y}}(\tilde{U}_y \tilde{B}^{(0)}) - \dot{\tilde{B}}^{(0)}$$

In Eq. (4), $\tilde{\eta} = \sigma_0/\sigma$ is the nondimensional magnetic diffusivity, R_m is the magnetic Reynolds number based upon $U_0 \sigma_0$, and a, and

$$\dot{\tilde{B}}^{(0)} = \frac{\partial \tilde{B}^{(0)}}{\partial \tilde{t}}$$

The current density components are

$$\tilde{J}_x = \mu_0^{-1} \frac{\partial \tilde{B}^{(i)}}{\partial \tilde{y}} \qquad \tilde{J}_y = -\mu_0^{-1} \frac{\partial \tilde{B}^{(i)}}{\partial \tilde{x}} \tag{5}$$

The boundary conditions appropriate to Eq. (4) are that on insulating boundaries,

$$\tilde{B}^{(i)} = \text{constant} \tag{6}$$

while on conductors

$$\frac{\partial \tilde{B}^{(i)}}{\partial \tilde{n}} = 0 \tag{7}$$

where $\tilde{n}$ is the normal coordinate to the conductor surface.

B. The Unsteady Flow Process

In the unsteady flow process, a plasmoid of initial breadth a_0 enters the magnetic field and electrode region at time t = 0. The front of the plasmoid moves at the shock-front velocity U_f. The fluid particles behind the shock front and beyond the contact surface move at the plasmoid velocity U_0. Within the plasmoid (demarked by the shock-front and contact surface), the electrical conductivity is σ_0, while outside the conductivity has the value $\sigma_\infty \ll \sigma_0$.

The applied magnetic field along the duct axis is assumed to be given by the following model profile function:

$$B^{(0)}(x) = B_m^{(0)} \begin{cases} 0 & |x| \le \frac{L}{2} \\ \dfrac{1+\exp(-\alpha L)-\exp[-\alpha(x+L/2)]}{[1-\exp(-\alpha L/2)]^2} - \dfrac{\exp[\alpha(x-L/2)]}{[1-\exp(-\alpha L/2)]^2} & |x| < \frac{L}{2} \end{cases} \qquad (8)$$

where $B_m^{(0)}$ is the maximum applied field. The values selected are L = 4h and α = 2/h where h is the duct height.

C. Resulting Electrical Distributions

Given an external load condition, and a given plasmoid gasdynamic condition we seek to describe the resulting current and induced magnetic field distributions as the plasmoid progresses through the MHD duct and generator section. We shall consider conditions for U_f/U_0 = 4/3 (corresponding to strong shocks in noble gases) and initial plasmoid breadths a_0/h = 1. The maximum nondimensional current flowing in the load circuit is $\bar{I} \equiv I/(\mu_0^{-1} B_m^{(0)} h)$ where I is the maximum current per unit length flowing to the external load.

The current streamline distributions (and corresponding induced magnetic field distribution) for a magnetic Reynolds number R_m = 10 are shown in Fig. 2. The complete dynamics of interaction between the generator current and the eddy-currents induced by the magnetic field distribution are revealed in Fig. 2.

III. Steady MHD Channel Flow at High R_m

A. Channel, Applied Magnetic Field, and Flow Configuration

We now consider the electrical conduction resulting from the steady flow of plasma at high magnetic Reynolds number in a constant area duct. The flows exist within the duct geometry and applied magnetic field distribution shown in Fig. 1 in which the generator electrode length is equal to the duct height. The applied magnetic field is given by Eq. (8).

The flow field has been calculated as that resulting from a reservoir which feeds the duct with argon at an inlet velocity of 10 km/sec, an internal energy of 37 MJ/kg, a pressure of 10 k bar, and a nominal electrical conductivity of 25,000 mho/m at the duct inlet. The resulting turbulent boundary layer interaction is considerable as the flow proceeds down the duct. These flow distributions have been calculated with the STD Research Corporation Q3D family of codes[4,5]

The generator electrodes are located at 0.6 m downstream from the duct entry from the driver. At the station 10 cm upstream from the generator inlet (x = 0.50 m) the conditions of the flow are

Velocity at duct centerline	9612 m/sec
Temperature at duct centerline	36,800 K
Mach number	3.14
Boundary layer thickness	5.5 mm

At the center of the generator section (x = 0.60 m) these values are

Velocity at duct centerline	9520 m/sec
Temperature at duct centerline	36,930 K
Mach number	3.11
Boundry layer thickness	6.5 mm

At the exit of the duct, (x = 0.70 m) these values are

Velocity at duct centerline	9430 m/sec
Temperature at duct centerline	36,970 K
Mach number	3.07
Boundary layer thickness	7.5 mm

This distribution of nonuniform velocity and temperature in x and y (with corresponding density and conductivity nonuniformity) resulting from the boundary layers is used as the basis for the electrical calculations utilizing Eq. (4). The nondimensionalized values are based upon the velocity and conductivity at the duct inlet (x = 0). The Reynolds number is based upon the channel height, h and has the value R_m = 7. The velocity and temperature profiles at various stations along the duct are shown in Fig. 4. Since these calculations decouple the electricity from the fluid behavior (weak or vanishing interaction) only the magnetic Reynolds number, R_m, is a relevant electrical parameter.

B. Resulting Electrical Distributions

The appropriate electrical equations to be solved are Eqs. (4) and (5) under steady state conditions. Boundary conditions are as given in Eqns. (6) and (7). The velocity and temperature profiles (and the corresponding electrical conductivity profile) will be similar to those shown in Fig. 3; however we shall reveal the effects of different absolute electrical conductivity levels (or velocity or size levels) by varying the magnetic Reynolds number for the various computed results.

In Fig. 4 we exhibit the open circuit and loaded condition for a magnetic Reynolds number R_m = 1. It can be seen that there is an onset of eddy cells induced in the regions of magnetic field gradients and a convection of the current pattern downstream of the generator. The principal generator current, however, is still confined to the region between the electrodes.

In Fig. 5 we exhibit the same situation but for a magnetic Reynolds number R_m = 7. We note that considerable current flow induced by the magnetic field gradients exists under open circuit conditions. Note how the upstream eddy cell actually couples into the generator electrodes. Under load, we see that the generator current exists completely downstream from the electrodes.

In Fig. 6 the conduction field for a magnetic Reynolds number R_m = 17.5 is shown.

Again, considerable eddy current activity exists both at open circuit and under load. The generator current is again driven out of the interelectrode gap and exists downstream of the electrodes.

IV. Three-Dimensional Strong Interaction Dynamics at High Magnetic Reynolds Number

A. Flow Structure Prediction in Hydromagnetic Channel Flow

In short burst MHD generator channel flow (timescale 100 μs ~ 1000 μs) utilizing explosively generated and compressed plasma as a stagnation source, the flow is very nearly a steady channel flow. At the plasma conditions of electrical conductivity, length scale, and velocities achievable in such flows both the interaction parameter I (ratio of Lorentz force to change of momentum) and magnetic Reynolds number R_m are large. For the hydromagnetic flows typical of the generators characterized by the operating conditions of Table 1 we find the magnetic Reynolds number R_m to be about 20 and the interaction parameter I to be about 15/meter. These conditions indicate that the deceleration time for the fluid is of the order of the diffusion time for the external magnetic field (consisting of applied and possible self-excited combinations) to penetrate through the plasma. One may therefore expect very significant interaction between the velocity field of the flow and the nonuniform Lorentz forces associated with the nonuniform magnetic field diffusion.

In Fig. 7 we indicate schematically the interaction of the magnetic field with the high R_m channel flow. Away from the front and throughout the channel, the lines are more sharply bent through the magnetic boundary layers and resemble the cross plane structure shown in Fig. 7. At high magnetic Reynolds number the magnetic boundary layers are thin and transverse gradients in y,z are much stronger than axial gradients in x. Correspondingly, the generator current is concentrated in the magnetic boundary layers. At the channel inlet the magnetic field is most strongly excluded from the flow; at the exit the field has penetrated most deeply. We now ask how a hydromagnetic flow will respond in its velocity, current, Lorentz force, and power generation distributions to this fundamental nonuniformity situation in high magnetic Reynolds Number, strong interaction flow.

TABLE 1

Conditions for Illustrative High Magnetic Reynolds Number Channel Flow

Generator Inlet Conditions	
$\langle U \rangle$	7×10^3 m/s
T	2.8×10^4 °K
p	3 k. bar
σ	5×10^4 mho/m
External Magnetic Field ($B^{(0)}$)	10 T
Generator Cross Section (h)	5 cm
R_m	22
I	15 m^{-1}

B. The Mathematical Model

The fluid mechanical evolution is calculated with the STD Research Corporation Q3D code family described in [4] and [5]. In the version of the Q3D family utilized in these calculations we center attention on the axial velocity field $U_x(x,y,z)$ and neglect the effects of the cross flow or secondary flow velocity field. Since I >> 1, the flow is dominated by electromagnetic rather than fluid mechanical viscous effects, although turbulent viscous effects are included in the calculation. Under conditions of I >> 1, R_m >> 1, it is possible to show that the transverse Lorentz force is of order $1/R_m$ times the axial Lorentz force. Hence, cross plane momentum is weakly generated by Lorentz forces compared to axial generation. The primary source of cross plane velocity nonuniformities is the redistribution of axial mass flow due to the nonuniform deceleration.

Let us now consider the electrical description. With $\bar{U} = (U_x, 0, 0)$, the three-dimensional induction equation can be expressed as

$$U_x \frac{\partial \bar{B}}{\partial x} = -\bar{B} \frac{\partial U_x}{\partial x} + \hat{x}(\bar{B} \cdot \nabla) U_x - \nabla \times (\eta \nabla \times \bar{B}) \qquad (9)$$

where $\hat{x}$ is the unit vector in the x-direction and $\eta = (\mu_0 \sigma)^{-1}$ is the magnetic diffusivity. The boundary conditions for $\bar{B}$ are as follows. As can be seen from Fig. 7, specifications of the boundary data for $\bar{B}$ on the channel perimeter requires solution of the external (outside the channel) as well as internal problem for $\bar{B}$. As an alternative to solution of the external problem, we approximate the boundary conditions for B_y, B_z as

$$\text{on } z = \pm \frac{w}{2} \begin{cases} B_y = \begin{cases} \mp (B_0 + \Delta B)\exp(-\lambda x) & y > 0 \\ \pm (B_0 + \Delta B)\exp(-\lambda x) & y < 0 \end{cases} \\ B_z = B_0 [1 - \exp(-\lambda x)] \end{cases} \qquad (10)$$

$$\text{on } y = \pm \frac{w}{2} \begin{cases} B_y = 0 \\ B_z = B_0 + \Delta B \exp(-\lambda x) \end{cases}$$

where $\lambda = \frac{4\pi^2 \eta}{\langle U \rangle} \frac{2}{w^2}$ is the decay term for the fundamental diffusion mode in a square duct, B_0 is the far-field external value of the magnetic field (totally in the z direction), and ΔB is the maximum compression of the magnetic field at the generator inlet. It can be seen that the approximate model (Eq. (10) possesses the correct limiting values at $x \to \infty$. For R_m >> 1, the values at $x \to 0$ are also close to the full-field exclusion solutions. The model is least accurate for conditions of $R_m \approx 1$.

For B_x the boundary conditions are $B_x = \pm \mu_0 I/2$ on $z = \pm w/2$ where I is the total current per unit depth flowing in the generator in the transverse direction.

C. Magnetic Diffusion and Flow Interaction

We now consider the predictions for flow in the generator channel of Fig. 7 under the conditions of Table 1. For these conditions we set the generator current at the nominal value

$$I = (1-K)\, w \langle \sigma u B_z \rangle$$

with K = 1/2 and w = the channel width. We assume that no field has penetrated the plasma at the electrode edge x = 0. (In general, one will expect a starting magnetic boundary layer thickness at the channel entrance dependent upon the plasma nozzle geometry and the fringe field location.)

The distribution of the transverse current J_y and the magnetic field component B_z for various axial stations in the channel are shown in Fig. 8. (There is an axially directed eddy current J_x associated with the fields B_z and B_y which is not shown here.) At x =

1.4 cm the magnetic boundary layers are exceedingly thin (≈ 3 mm). They have grown to 1.4 cm at x = 14 cm and 2.9 cm at x = 28 cm. The inward diffusing magnetic field component B_z is initially concentrated along the walls parallel to the external magnetic field (electrode walls; see Fig. 1), but the z component on the side walls builds up as the flow proceeds down the channel. The transverse current J_y is initially concentrated along the sidewalls and diffuses inward from these walls.

In Fig. 9 we observe the impact of these distributions of current and magnetic field on Lorentz force and axial velocity. In the early stages of the flow evolution the maximum axial Lorentz force is an the corners. This is because the maximum field B_z exists on the electrode walls parallel to the z axis and maximum current J_y exists on the sidewalls parallel to the y axis. The maximum product of the two therefore exists in the corners. Throughout the entire evolution, the maximum Lorentz force is concentrated in the magnetic boundary layers along the sidewalls.

The impact on the velocity distribution is strong and significant. The initially flat velocity profile is rapidly decelerated in the sidewall layers. By 12 cm the flow is actually reversed in the corners and the regions of reverse flow spread. Because of the deceleration of the wall regions by the inward diffusing Lorentz force the core flow is accelerated. From an initial value of 7 km/s the core flow is accelerated to nearly 10 km/s by x = 28 cm. Since there is little Lorentz force in the core region, this high velocity region is not effectively coupled by the generator.

It should be noted that once reverse flow occurs (stalled MHD boundary layers) the present prediction of the actual velocity field in the wall layer region cannot be considered correct since upstream feedback is prohibited by the method of calculation. The present calculation is only definitive in its prediction that stall will indeed occur. In actuality we conjecture that the flow under these conditions will appear as shown in Fig. 10 in which recirculation eddies are trapped within the boundary layer region of intense Lorentz force while the core flow jets through outside the region of the eddies. In such a stalled flow, there is little Lorentz force coupling to the high momentum jet in the central region of the channel.

As a demonstration that stall is not a peculiarity of the corner region, we show the Lorentz force and velocity profiles at x_3 = 21 cm for a higher interaction situation ($\sigma = 2 \times 10^3$ mho/m) but otherwise conditions identical to Table 1 (Fig.11). In Fig. 12 we see that the entire sidewall has reversed flow under these conditions.

In Fig. 13 we show the distribution of power production $-(\vec{J} \cdot \vec{E})$ over the cross section. Power is only produced in the mid-wall layer regions and is actually consumed in the corner and sidewall layers where reversed flow takes place. The overall power extraction per unit length, dP/dx, is defined as the integral of the power density over the channel cross section:

$$\frac{dP}{dx} = -\int_A \int (\vec{J} \cdot \vec{E})\, d^2x$$

The ideal power extraction for uniform flow is

$$\left(\frac{dP}{dx}\right)_{ideal} = K(1-K)\sigma u_0^2 B_0^2 A$$

In Fig. 14 we exhibit the ratio of these quantities for the conditions of Table 1. It can be seen that for a channel 15 cm long, only 10% of the ideal power is available and for a 28 cm channel only 27% is available. These results must be tempered by the observation that beyond 12 cm the boundary layers have begun to stall; it is not likely that power extraction will be enhanced by realistic inclusion of the recirculation zones under stalled conditions. Hence, the power extraction levels beyond x = 12 cm will likely not be reached.

V. Acknowledgement

The authors would like to acknowledge many interesting discussions of this problem with S. T. Demetriades and C. D. Bangerter. This work was supported by the U.S. Office of Naval Research under Contract ONR-N-00013-77-C-0574.

References

1. C. D. Bangerter and B. D. Hopkins, Hercules, Inc., and T. R. Brogan, MEPPSCO, Inc., Proc. 6th Int'l. Conf. on Magnetohydrodynamic Electrical Power Generation, Vol. IV, p. 155, Washington, D.C., June 1975

2. S. P. Gill, D. W. Baum, and H. Calvin, "Explosive MHD Research," Artec Assoc., Annual Rpt. No. 119AR to ONR, April 1975 - April 1976

3. T. F. Swean, C. D. Bangerter and D. M. Markham, "Dynamics of Strong Interaction Shock-Generated Plasma," Paper No. AIAA-80-0027, AIAA 18th Aerospace Sciences Meeting, Pasadena, Calif., January 1980

4. S. T. Demetriades, G. S. Argyropoulos, C. D. Maxwell, "Progress in Analytical Modeling of MHD Power Generators," Proc., 12th Symposium on Engineering Aspects of Magnetohydrodynamics, Argonne Nat'l. Lab., Argonne, IL, pp. I.5.1-I.5.12, March 1972

5. STD Research Corporation, "STD/MHD Codes Introductory User's Guide; Code: QUE3DEE, Family: Q3D, Rpt. No. STDR-102-79, July 1979

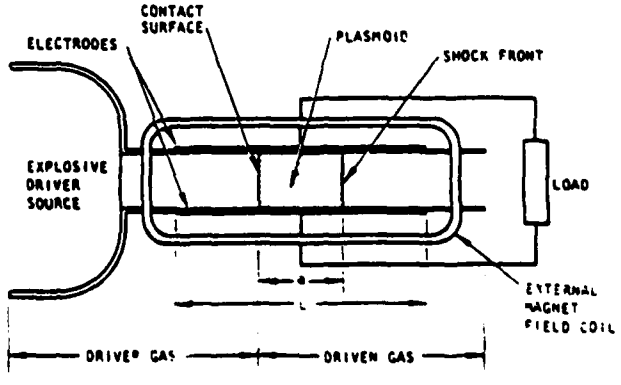

9-2974

Fig. 1. Schematic of explosion driven plasmoid flow.

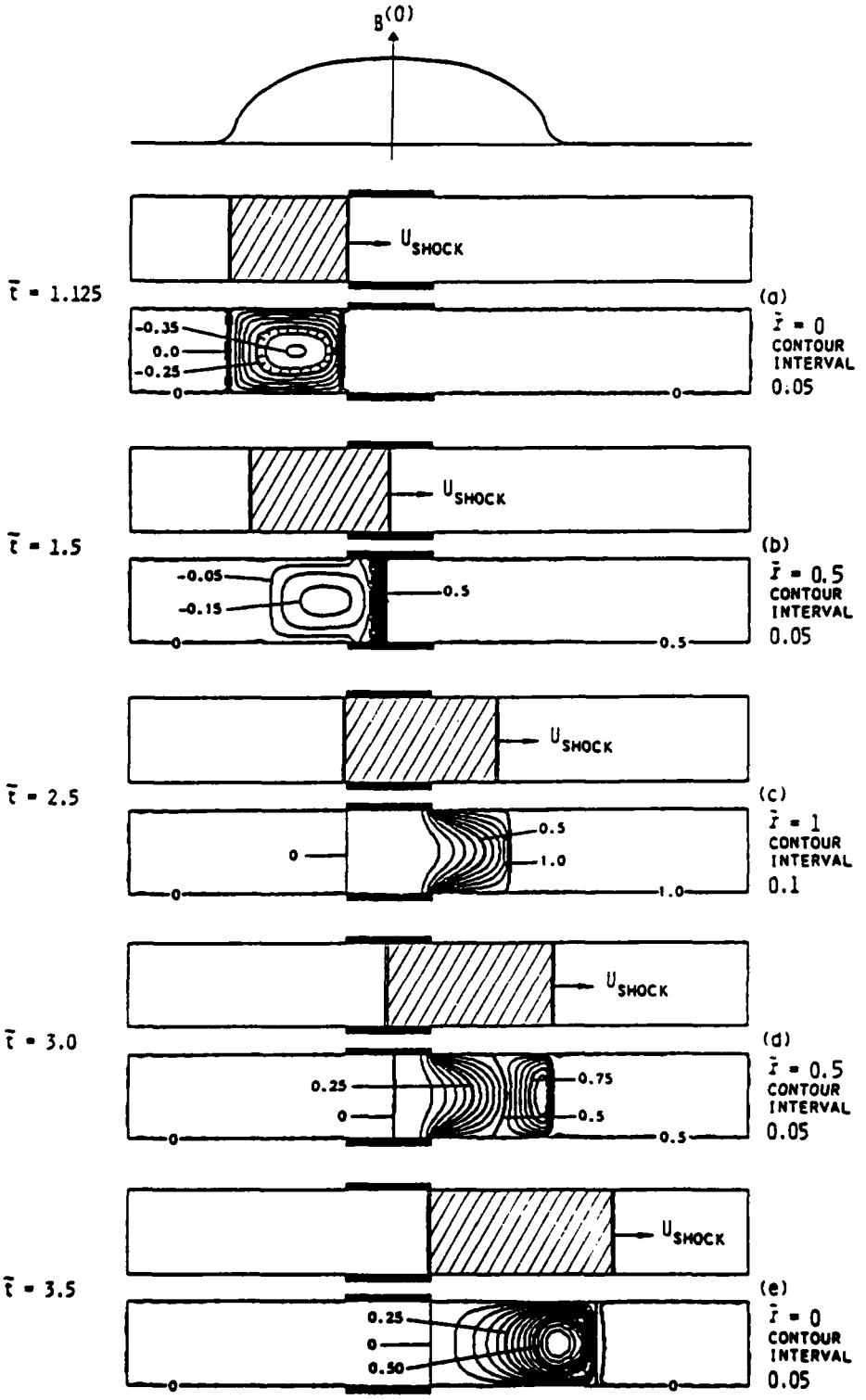

0-3589

Fig. 2. Induced magnetic field isolevels (current density streamlines) at R_m = 10 in unsteady passage of explosion-driven plasmoid. At time t = 0, the shock front is at the "edge" of the applied magnetic field. Upper figure in each time sequence indicates plasmoid position. Lower figure indicates magnetic field isolevels. Note intense eddy-current cells in (a) and (e) when plasmoid is in region of applied magnetic field gradient and out of range of electrodes. In (b), the generator current is concentrated in a thin zone behind the shock front. In (c), the plasmoid has progressed downstream so that the generator current is strongly convected downstream. In (d), the generator current and downstream eddy cell interact together.

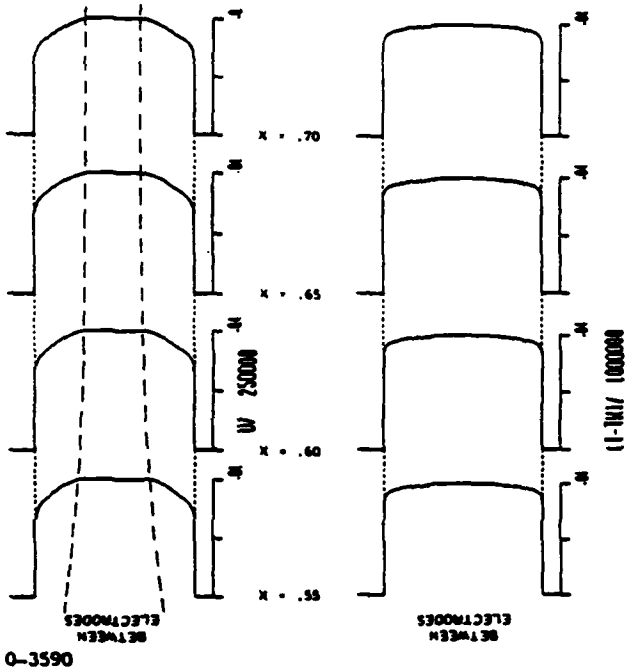

0-3590

Fig. 3. Velocity and temperature profiles between electrodes in turbulent supersonic plasma flow in an MHD generator duct.

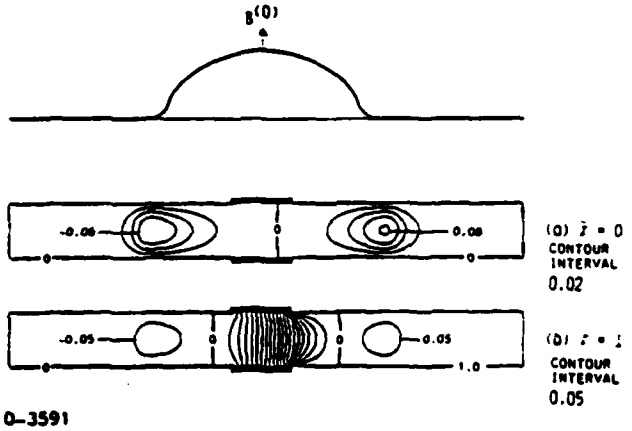

0-3591

Fig. 4. Induced magnetic field isolevels $\tilde{B}^{(i)}$ for steady magnetohydrodynamic flow with profiles similar to those of Fig. 3 and $R_m = 1$. In (a), the generator is at open circuit ($\tilde{I} = 0$) and in (b) the generator is under load ($\tilde{I} = 1$).

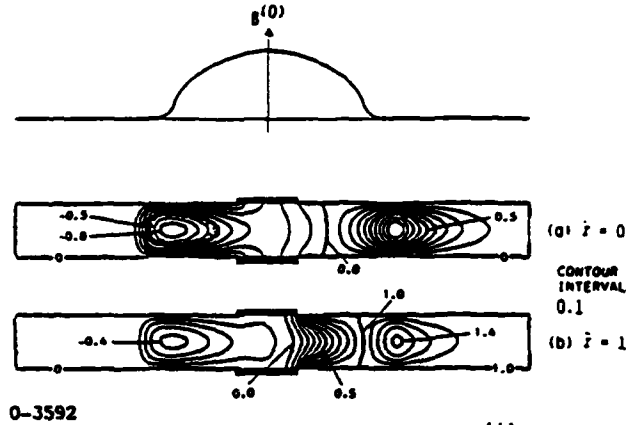

0-3592

Fig. 5. Induced magnetic field isolevels $\tilde{B}^{(i)}$ for steady magnetohydrodynamic flow with the profiles of Fig. 3 and $R_m = 7$. In (a), the generator is at open circuit ($\tilde{I} = 0$) and in (b) the generator is under load ($\tilde{I} = 1$).

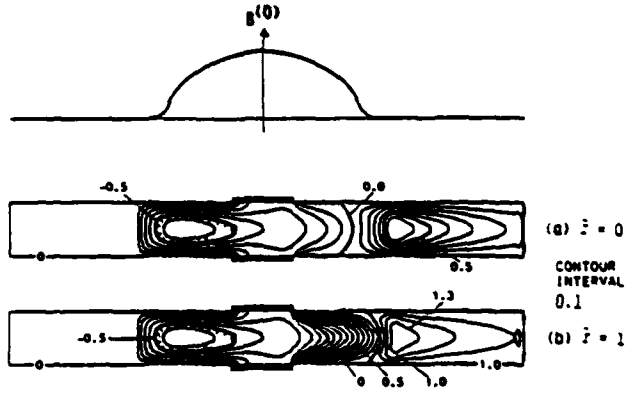

0-3593

Fig. 6. Induced magnetic field isolevels $\tilde{B}^{(i)}$ for steady magnetohydrodynamic flow with profiles similar to those of Fig. 3 and $R_m = 17.5$. In (a), the generator is at open circuit ($\tilde{I} = 0$) and in (b) the generator is under load ($\tilde{I} = 1$).

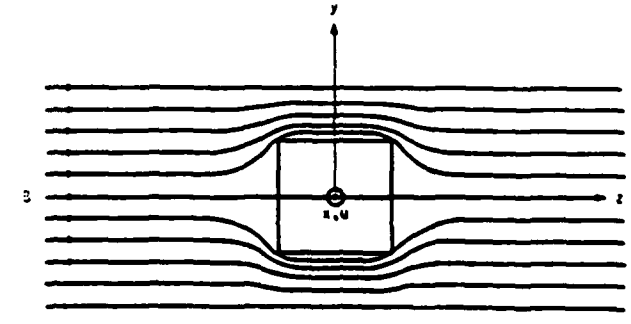

...structure of Magnetic Field ...
...romagnetic Channel Flow

8-2870

Fig. 7. Magnetic field nonuniformities in High Magnetic Reynolds Number channel flow.

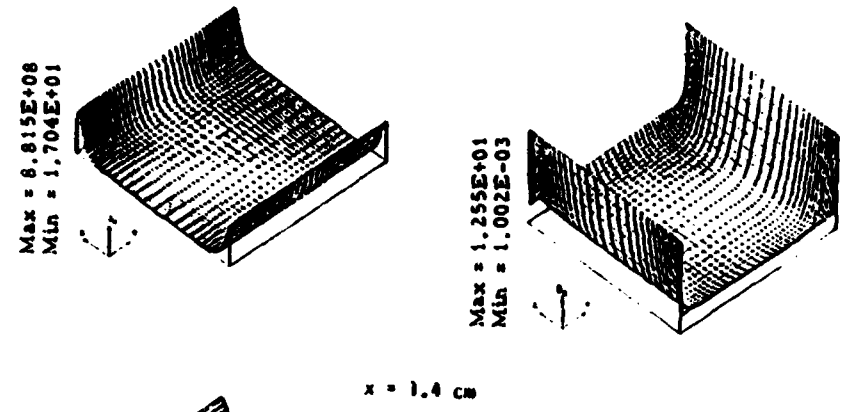

x = 1.4 cm

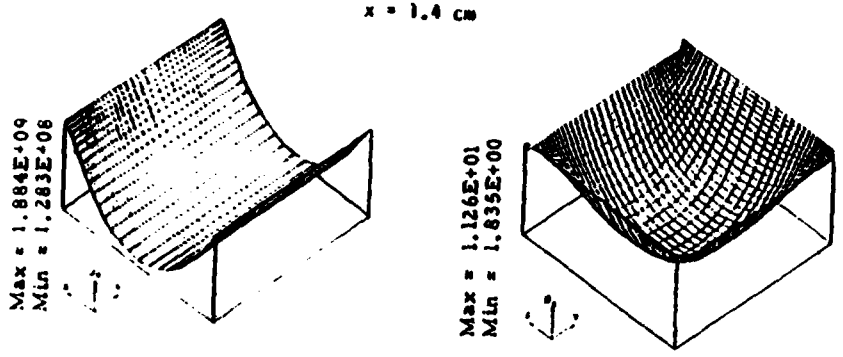

x = 14 cm

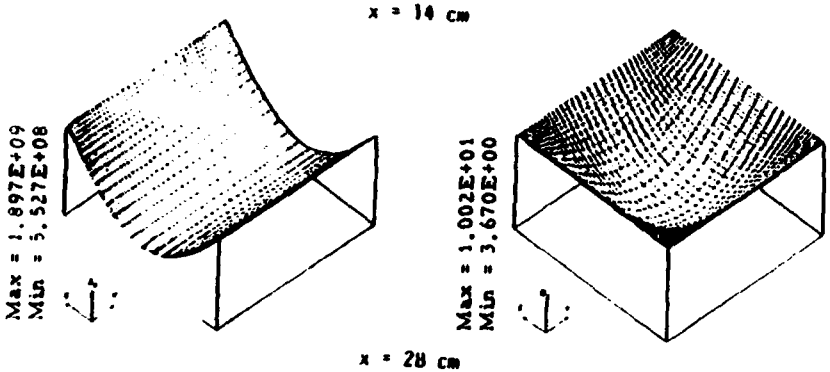

x = 28 cm

H-2871

Fig. 8. Transverse current and external magnetic field distribution at three axial stations in high Magnetic Reynolds Number channel flow.

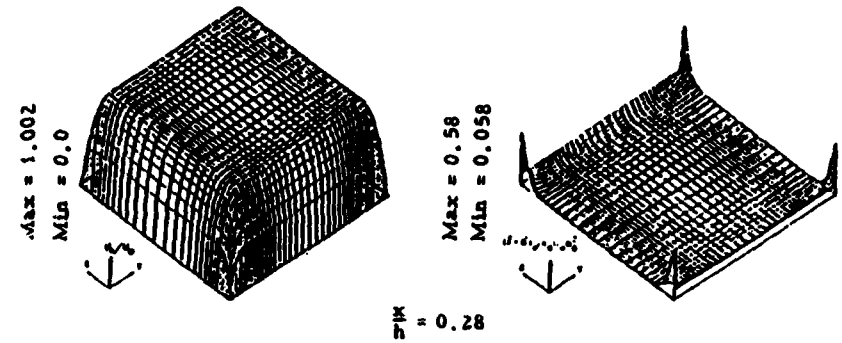

x = 0.28

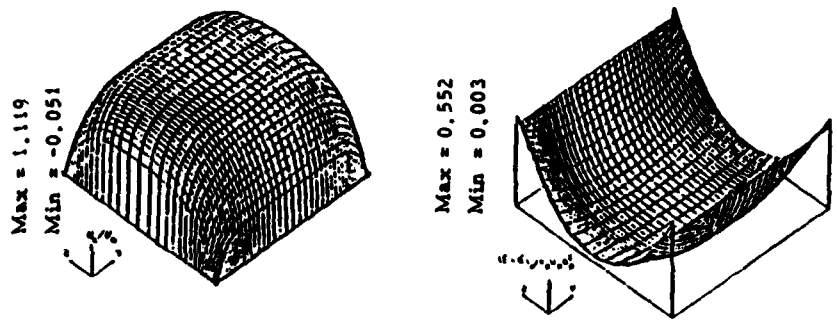

x = 2.80

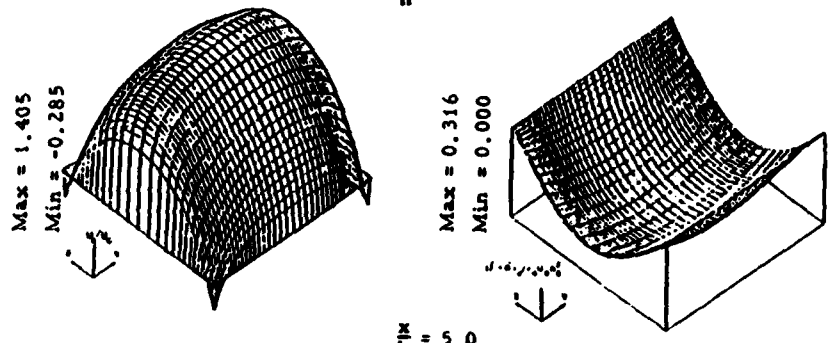

x = 5.0

Fig. 9. Lorentz force and axial velocity distributions at three axial stations in high magnetic reynolds number channel flow. wall layers are sharply decelerated with wall layer flows actually reversing. Core flow is accelerated.

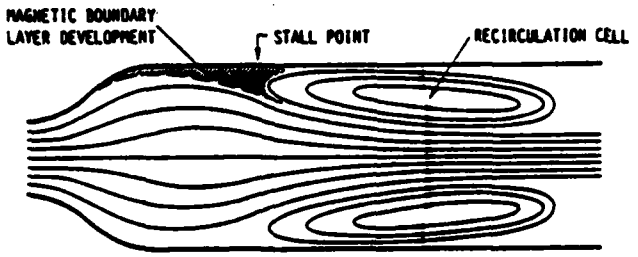

0-3594

Fig.10. Conjectured velocity streamlines in stalled high Magnetic Reynolds Number channel flow showing recirculation cells trapped in boundary layer region.

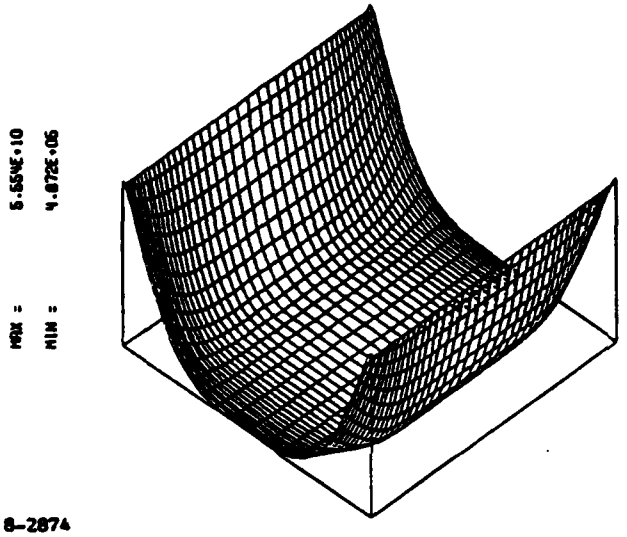

8-2874

Fig.11. Lorentz force distribution at x = 21 cm corresponding to higher interaction case (σ = 2 x 10^5 mho/m) but otherwise conditions as in Table 1.

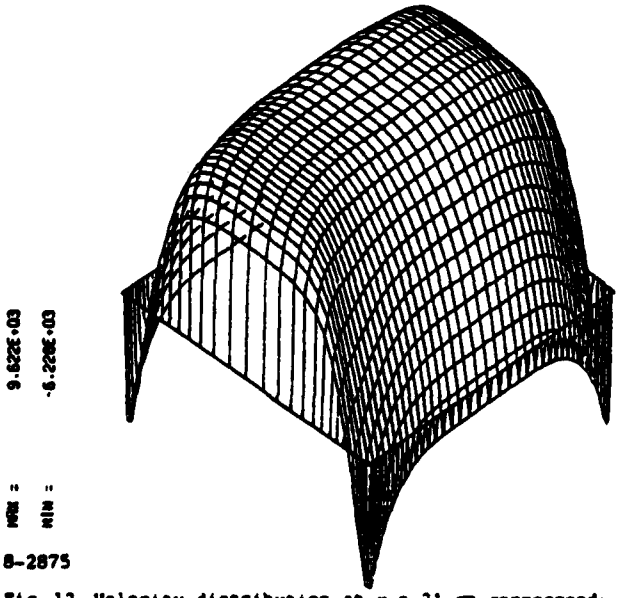

8-2875

Fig. 12. Velocity distribution at x = 21 cm corresponding to a higher interaction case (σ = 2 x 10^5 mho/m) but otherwise conditions as in Table 1. Note that entire sidewall flow is reversed in this case.

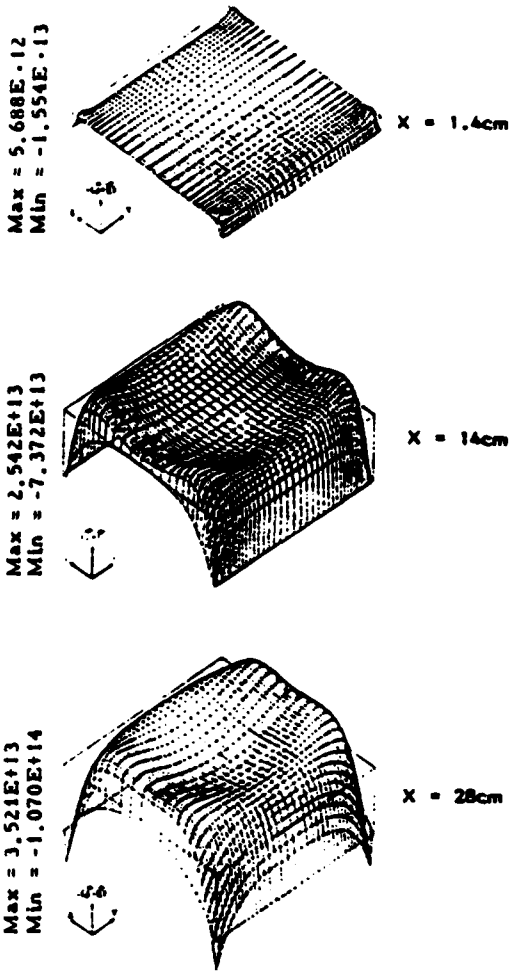

8-2876

Fig.13. Power extraction density evolution for the case in Figs. 2 and 3. Power is produced in mid-wall layer and core regions but consumed in near wall regions.

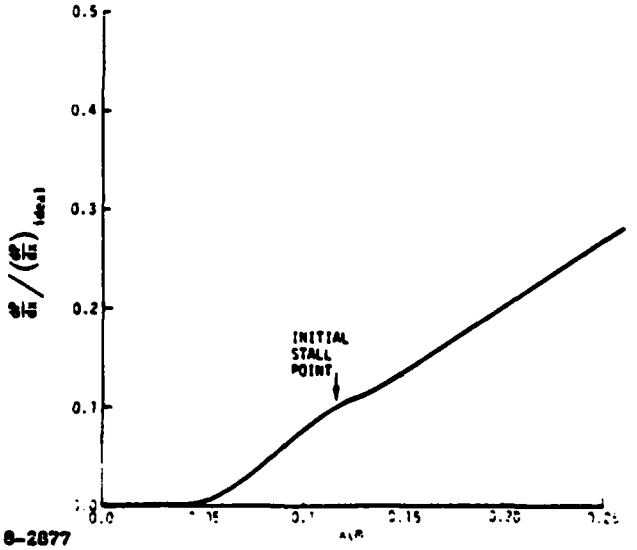

8-2877

Fig. 14. Ratio of power extraction per unit length to ideal power extraction. Wall layers stalled over most of channel length.